

6-26-2015

# The Electroreduction of Carbon Dioxide on Porous Copper Nanoparticles

Monica Alisa Padilla

Follow this and additional works at: [https://digitalrepository.unm.edu/cbe\\_etds](https://digitalrepository.unm.edu/cbe_etds)



Part of the [Chemical Engineering Commons](#)

---

## Recommended Citation

Padilla, Monica Alisa. "The Electroreduction of Carbon Dioxide on Porous Copper Nanoparticles." (2015).  
[https://digitalrepository.unm.edu/cbe\\_etds/47](https://digitalrepository.unm.edu/cbe_etds/47)

This Thesis is brought to you for free and open access by the Engineering ETDs at UNM Digital Repository. It has been accepted for inclusion in Chemical and Biological Engineering ETDs by an authorized administrator of UNM Digital Repository. For more information, please contact [disc@unm.edu](mailto:disc@unm.edu).

Monica Alisa Padilla

---

*Candidate*

Chemical and Biological Engineering

---

*Department*

This thesis is approved, and it is acceptable in quality and form for publication:

*Approved by the Thesis Committee:*

Plamen Atanassov , Chairperson

---

Abhaya Datye

---

Alexey Serov

---

---

**THE ELECTROCHEMICAL REDUCTION OF  
CARBON DIOXIDE ON POROUS  
COPPER NANOPARTICLES**

by

**MONICA ALISA PADILLA**

**BACHELORS OF FINE ARTS IN ART STUDIO  
BACHELORS OF SCIENCE IN CHEMICAL ENGINEERING  
MASTERS OF SCIENCE IN CHEMICAL ENGINEERING**

THESIS

Submitted in Partial Fulfillment of the  
Requirements for the Degree of

**Masters of Science  
Chemical Engineering**

The University of New Mexico  
Albuquerque, New Mexico

**May, 2015**

## Dedication

This work is dedicated to my dad- you finally got your engineer.

## Acknowledgements

I would like to thank the members of my committee for their time and beneficial feedback in the development of this thesis: Dr. Plamen Atanassov, Dr. Alexey Serov, and Dr. Abhaya Datye.

I would like to additionally thank Dr. Plamen Atanassov for his guidance and continuous support in my education for the past five years; your vision and leadership are inspiring.

I would like to additionally thank Dr. Alexey Serov for sharing his extensive knowledge of chemistry with me and for including me in many, many materials development projects; learning by doing was incredibly valuable.

I would like to thank Dr. Olga Baturina for her guidance on the topic of carbon dioxide electroreduction.

I would like to acknowledge the significant contributions to my understanding of engineering taught to me during my undergraduate and graduate studies by the following professors at the University of New Mexico: Dr. Eric Carnes, Dr. Sang M. Han, Dr. Dimeter Petsev, and Dr. Timothy Ward.

I would like to appreciate the benefits of assistance from and discussions with Dr. Ulises Martinez and Aaron Roy.

I would like to thank Mabel Padilla for editing many drafts of this thesis – your keen eye for detail is priceless.

And finally, I would like to extend a heartfelt thanks to my family and friends without whom I would not have the perspective to overcome the numerous challenges I encountered during my pursuit of this degree. It is my sincere hope that I will be able to return a favor of comparable magnitude to each of you.

# **The Electroreduction of Carbon Dioxide on Porous Copper Nanoparticles**

**by**

**Monica Alisa Padilla**

**B.F.A., Art Studio, University of New Mexico, 2002**

**B.S., Chemical Engineering, University of New Mexico, 2013**

**M.S., Chemical Engineering, University of New Mexico, 2015**

## **ABSTRACT**

Copper nanoparticles of porous, controlled structure were synthesized using the sacrificial support method (SSM). The precursor weight percent (wt%) of copper (Cu) and fumed silica (EH-5) was varied to determine the optimum ratio for this material. The precursors were reduced at i) 350°C in a 7% H<sub>2</sub> atmosphere and ii) at 250°C in a 100% H<sub>2</sub> atmosphere. The specific surface areas of the nanoparticles was measured by Brunauer-Emmett-Teller N<sub>2</sub> absorption. The morphologies and widths of the nanoparticles were confirmed by imaging the nanoparticles by scanning electron microscopy (SEM). The bulk composition of the nanoparticles was determined by X-ray diffraction (XRD). Results of these characterizations are discussed in detail. The nanoparticles with a precursor Cu content of 5 and 10wt% exhibited the most controlled morphology with smallest particle widths when reduced at 250°C in 100% H<sub>2</sub> (21.5 ± 6.7 nm and 29.3 ±

11.3 nm, respectively) and at 350°C in 7% H<sub>2</sub> (29.8 ± 9.4 nm and 60.5 ± 21.5 nm, respectively).

Carbon dioxide (CO<sub>2</sub>) electroreduction (CER) on the Cu nanoparticles synthesized by SSM was confirmed with rotating disk electrode experiments (RDE) using cyclic voltammetry at 25°C in CO<sub>2</sub> saturated 0.1M potassium bicarbonate solution (KHCO<sub>3</sub>) at atmospheric pressure. The electrochemical stability of these nanoparticles was tested via bulk electrolysis for one hour at -1.2, -1.6, and -2.2 V vs. Ag/AgCl in kinetic and diffusion limited regimes. All nanoparticles exhibited activity towards CER and displayed excellent stability for at the potentials tested. The current densities observed during bulk electrolysis at -2.2 V vs. Ag/AgCl were between ca. -23 and -40 mA cm<sup>-2</sup> for the nanoparticles reduced at 350 °C in 7% H<sub>2</sub> atmosphere and ca. -12 and -20 mA cm<sup>-2</sup> for the nanoparticles reduced at 250°C in 100% H<sub>2</sub> atmosphere. The magnitude and stability of these particles makes them ideal candidates for further studies that will determine their relative efficiencies towards specific CER products by liquid and gas quantification.

## Table of Contents

<b>List of Figures</b> -----	ix
<b>List of Tables</b> -----	xii
<b>1. Introduction</b> -----	1
1.1 Statement of intent-----	4
<b>2. Background</b> -----	6
2.1 Carbon dioxide electroreduction on metals-----	6
2.2 Carbon dioxide electroreduction on copper-----	7
2.2.1 Measures of merit: efficiency and selectivity-----	7
2.2.2 Overpotential and the mechanism of carbon dioxide electroreduction-----	9
2.2.3 Influence of copper surface structure on selectivity-----	12
2.2.4 Modifications to copper: influence of alloying and conductive supports-----	13
2.3 Copper nanoparticles: challenges in material synthesis-----	14
2.4 Electrolyte-----	16
2.4.1 The limited solubility of carbon dioxide in solution and the effect of pressure-----	16
2.4.2 The effect of solution pH-----	17
2.4.3 Deactivation of copper by trace metals-----	19
2.5 Temperature-----	19
2.6 Further considerations for integration into application-----	20
<b>3. Experimental Methods</b> -----	23
3.2 Synthesis of Cu nanoparticles-----	23
3.3 Characterization-----	24
3.3.1 Material characterization-----	24
3.3.2 Electrochemical characterization-----	24
<b>4. Results and Discussion</b> -----	26
4.1 Characterization-----	26
4.1.1 Scanning electron microscopy-----	26
4.1.2 Brunauer-Emmett-Teller surface area-----	29
4.1.3 X-ray diffraction-----	30
4.2 Electrochemical characterization-----	32
4.2.1 Cyclic voltammetry-----	32



4.2.2 Bulk electrolysis	36
4.3 Correlations between electrochemical performance material properties	41
<b>5. Conclusions</b>	<b>46</b>
<b>APPENDICES</b>	<b>48</b>
<b>Appendix 1.</b> Particle size, defined as the length of the chord for non-spherical particles and diameter for spherical particles, distributions of Cu nanoparticles synthesized using the SSM, as determined by SEM.	48
<b>Appendix 2.</b> XRD patterns taken of Cu nanoparticles synthesized using the SSM.	50
<b>Appendix 3.</b> Confirmation of CO <sub>2</sub> electroreduction on Cu nanoparticles with cyclic voltammetry at 20 mV s <sup>-1</sup> in N <sub>2</sub> and CO <sub>2</sub> saturated 0.1M KHCO <sub>3</sub> solutions.	53
<b>Appendix 4.</b> Bulk electrolysis for carbon dioxide electroreduction of Cu nanoparticles held for one hour at -1.6 and -2.2 V vs. Ag/AgCl in 0.1M KHCO <sub>3</sub> , without rotation.	55
<b>References</b>	<b>56</b>

## List of Figures

<b>Figure 1.</b> Projected changes in precipitation and temperature modeled from current atmospheric conditions without greenhouse gas reduction. On the left are trends observed from 1865-1875, on the right are predictions for 2045-2055 [5]. -----	1
<b>Figure 2.</b> Survey of current densities (CD) of CO <sub>2</sub> reduction reported from 1985 to 2012 as compiled by Jhong et al. shows a) faradaic efficiencies (FE) towards three major products (CO, CH <sub>4</sub> , HCOOH) and b) energy efficiencies (EE), exhibiting the lack of catalysts that exhibit both high CD and high FE or EE [33].-----	4
<b>Figure 3.</b> A graph depicting the range of products and their faradaic efficiencies for CO <sub>2</sub> reduction on Cu as a function of potential, generated and reported by Hori et al. Total faradaic efficiency is depicted in the top segment [22].-----	10
<b>Figure 4.</b> The effect of pH on product distribution for KHCO <sub>3</sub> solutions varied from 0.03 to 1.5M where: □ -H <sub>2</sub> , Δ -C <sub>2</sub> H <sub>4</sub> , ◇ -C <sub>2</sub> H <sub>5</sub> OH, ○ -CH <sub>4</sub> , Δ <sup>-1</sup> - C <sub>3</sub> H <sub>7</sub> OH [22].-----	18
<b>Figure 5.</b> The Pourbaix diagram for Cu in aqueous solutions; note the phase boundary between Cu and Cu <sub>2</sub> O exists near 0 V vs. SHE at pHs 9-10 [72].-----	19
<b>Figure 6.</b> SEM images of Cu nanoparticles synthesized at 350 °C in a 7% H <sub>2</sub> reduction atmosphere: a) Cu <sub>A1</sub> , b) Cu <sub>A2</sub> , c) Cu <sub>A3</sub> , d) Cu <sub>A4</sub> , and e) Cu <sub>A5</sub> . The Cu <sub>A1</sub> & Cu <sub>A2</sub> particles (a-b) exhibit sponge-like morphology consistent with the sacrificial support method (voids from EH-5 indicated in red).-----	28
<b>Figure 7.</b> SEM images of the Cu nanoparticles synthesized at 250 °C in a 100% H <sub>2</sub> reduction: a) Cu <sub>B1</sub> , b) Cu <sub>B2</sub> , c) Cu <sub>B3</sub> , d) Cu <sub>B4</sub> , and e) Cu <sub>B5</sub> . The Cu <sub>B1</sub> , Cu <sub>B2</sub> , Cu <sub>B3</sub> , and Cu <sub>B4</sub> particles (a-d) exhibit sponge-like morphology consistent with the sacrificial support method (voids from EH-5 indicated in red).-----	28
<b>Figure 8.</b> The effect of precursor Cu weight percent (wt%) on the average particle width during synthesis using the sacrificial support method.-----	29
<b>Figure 9.</b> The effect of the precursor Cu weight percent and the reduction environment on the final Cu <sup>0</sup> content in the particles prepared using the sacrificial support method where a) 100% H <sub>2</sub> (250°C) and b) 7% H <sub>2</sub> (350°C). -----	30
<b>Figure 10.</b> The cathodic sweep of voltammograms performed at 1 mV s <sup>-1</sup> of Cu particles synthesized using SSM in 7% H <sub>2</sub> at 350°C (Cu <sub>AX</sub> , where X=1-5). Conditions: 0.1M KHCO <sub>3</sub> , 25°C, no rotation.-----	33
<b>Figure 11.</b> The cathodic sweep of voltammograms performed at 1 mV s <sup>-1</sup> of Cu particles synthesized using SSM in 100% H <sub>2</sub> at 250°C. (Cu <sub>BX</sub> , where X=1-5). Conditions: 0.1M KHCO <sub>3</sub> , 25°C, no rotation.-----	33
<b>Figure 12.</b> Comparison of average current densities from particles reduced in a) Cu <sub>AX</sub> and b) Cu <sub>BX</sub> (X=1-5) for bulk electrolysis and slow scan voltammetry at -1.6 V vs. Ag/AgCl illustrating the discrepancies between expected and observed steady state values. -----	37
<b>Figure 13.</b> Bulk electrolysis of Cu particles reduced at 350°C in a 7% H <sub>2</sub> atmosphere at a) -1.6 and at b) -2.2 V vs. Ag/AgCl. Conditions: 0.1M KHCO <sub>3</sub> , 1600 RPM, 25 °C.-----	38
<b>Figure 14.</b> Bulk electrolysis of Cu particles reduced at 250°C in a 100% H <sub>2</sub> atmosphere at a) -1.6 and at b) -2.2 V vs. Ag/AgCl. Conditions: 0.1M KHCO <sub>3</sub> , 1600 RPM, 25°C.-----	40

- Figure 15.** Cu particles synthesized in 7% H<sub>2</sub> at 350°C exhibit decreasing current density as Cu<sup>0</sup> content increases at -1.2 (top) and -2.2 (bottom), with no apparent correlation at -1.6 (middle) V vs. Ag/AgCl. Conditions: 0.1M KHCO<sub>3</sub>, 1600 RPM, 25°C. -----42
- Figure 16.** Cu particles synthesized in 7% H<sub>2</sub> at 350°C exhibit increasing current density for increasing BET surface area at -1.2 (top) and -2.2 V vs. Ag/AgCl (bottom), with no clear effect at -1.6 (middle) V vs. Ag/AgCl. Conditions: 0.1M KHCO<sub>3</sub>, 1600 RPM, 25°C. -----42
- Figure 17.** Cu particles synthesized in 100% H<sub>2</sub> at 250°C exhibit decreasing current for increasing Cu<sup>0</sup> content at -2.2 (bottom), with no apparent correlation at -1.2 (top) and -1.6 (middle) V vs. Ag/AgCl. Conditions: 0.1 M KHCO<sub>3</sub>, 1600 RPM, 25°C. -----43
- Figure 18.** Cu particles synthesized in 100% H<sub>2</sub> at 250°C exhibit decreasing current density for increasing BET surface area at -1.2 (top) and -1.6 (middle), with near clear effect at -2.2 (bottom) V vs. Ag/AgCl. Conditions: 0.1 M KHCO<sub>3</sub>, 1600 RPM, 25 °C.-----43
- Figure 19.** Particle width distributions of Cu synthesized in 7% H<sub>2</sub> at 250°C: a) Cu<sub>A1</sub>, b) Cu<sub>A2</sub>, c) Cu<sub>A3</sub>, d) Cu<sub>A4</sub>, e) Cu<sub>A5</sub>. The Cu<sub>A1</sub>, Cu<sub>A2</sub>, and Cu<sub>A3</sub> particles appear to have a normal distribution (a-c); Cu<sub>A4</sub> (d) is skewed left and exhibits two populations at ca. 60 and 118, while Cu<sub>A5</sub> (e) similarly exhibits a skewed left distribution with two populations at ca. 55 nm and 95 nm.-----48
- Figure 20.** Particle width distributions of Cu synthesized in 100% H<sub>2</sub> at 350 °C: a) Cu<sub>B1</sub>, b) Cu<sub>B2</sub>, c) Cu<sub>B3</sub>, d) Cu<sub>B4</sub>, e) Cu<sub>B5</sub>. The Cu<sub>B1</sub> and Cu<sub>B2</sub> (a-b) particles appear to have a normal distribution. The Cu<sub>B3</sub>, Cu<sub>B4</sub>, and Cu<sub>B5</sub> (c-e) distributions are skewed left, but exhibit singular population means (ca. 40, 45, and 75 nm respectively).-----49
- Figure 21.** XRD patterns of catalysts prepared from 5wt% Cu precursors in 7% (Cu<sub>A1</sub>, red) and 100% H<sub>2</sub> (Cu<sub>B1</sub>, black) atmospheres. Cu<sub>2</sub>O (squares): 29.6° - (110), 36.4° - (111), 42.3° - (200), 61.4° - (220). Cu (circles): 43.2° - (111), 50.4° - (200). CuO is a minor phase included in refinements for the particles reduced in 7% H<sub>2</sub>, at 12.7mol%.-----50
- Figure 22.** XRD patterns of catalysts prepared from 10wt% Cu precursors in 7% (Cu<sub>A2</sub>, red) and 100% H<sub>2</sub> (Cu<sub>B2</sub>, black) atmospheres. Cu<sub>2</sub>O (squares): 29.6° - (110), 36.4° - (111), 42.3° - (200), 61.4° - (220). Cu (circles): 43.2° - (111), 50.4° - (200). CuO is a minor phase included in refinements for the particles reduced in 7% H<sub>2</sub> and 100% H<sub>2</sub>, at 1.58 at 8.47 mol%, respectively. -----50
- Figure 23.** XRD patterns of catalysts prepared from 20wt% Cu precursors in 7% (Cu<sub>A3</sub>, red) and 100% H<sub>2</sub> (Cu<sub>B3</sub>, black) atmospheres. Cu<sub>2</sub>O (squares): 29.6° - (110), 36.4° - (111), 42.3° - (200), 61.4° - (220). Cu (circles): 43.2° - (111), 50.4° - (200). CuO is a minor phase included in refinements for the particles reduced in 100% H<sub>2</sub>, at 12.1 mol%.-----51
- Figure 24.** XRD patterns of catalysts prepared from 30wt% Cu precursors in 7% (Cu<sub>A4</sub>, red) and 100% H<sub>2</sub> (Cu<sub>B4</sub>, black) atmospheres. Cu<sub>2</sub>O (squares): 29.6° - (110), 36.4° - (111), 42.3° - (200), 61.4° - (220). Cu (circles): 43.2° - (111), 50.4° - (200). CuO was not detected as a minor phase. -----51
- Figure 25.** . XRD patterns of catalysts prepared from 40wt% Cu precursors in 7% (Cu<sub>A5</sub>, red) and 100% H<sub>2</sub> (Cu<sub>B5</sub>, black) atmospheres. Cu<sub>2</sub>O (squares): 29.6° - (110), 36.4° - (111), 42.3° - (200), 61.4° - (220). Cu (circles): 43.2° - (111), 50.4° - (200). CuO is a minor phase included in refinements for the particles reduced in 7% H<sub>2</sub>, at 4.61 mol%. -----52
- Figure 26.** Confirmation of CER activity by comparison of cathodic voltammograms of Cu nanoparticles reduced at 350 °C in 7% H<sub>2</sub>. Conditions: N<sub>2</sub> or CO<sub>2</sub> saturated 0.1M KHCO<sub>3</sub>, 1600 RPM, 25°C. Particles are as follows: a) Cu<sub>A1</sub>, b) Cu<sub>A2</sub>, c) Cu<sub>A3</sub>, d) 3 Cu<sub>A4</sub>, and e) Cu<sub>A5</sub>. -----53

**Figure 27.** Confirmation of CER activity by comparison of cathodic voltammograms of Cu nanoparticles reduced at 250°C in 100% H<sub>2</sub>. Conditions: N<sub>2</sub> or CO<sub>2</sub> saturated 0.1M KHCO<sub>3</sub>, 1600 RPM, 25°C. Particles are as follows: a) Cu<sub>B1</sub>, b) Cu<sub>B2</sub>, c) Cu<sub>B3</sub>, d) 3 Cu<sub>B4</sub>, and e) Cu<sub>B5</sub>. -----54

**Figure 29.** Bulk electrolysis of Cu<sub>BX</sub> (X=1-5) particles reduced at 250°C in a 100% H<sub>2</sub> atmosphere at a) -1.6 and at b) -2.2 V vs. Ag/AgCl. Conditions: 0.1 M KHCO<sub>3</sub>, 1600 RPM, 25°C. Large spikes in current densities are caused by coverage of the working electrode surface by gas. -----55

**Figure 28.** Bulk electrolysis of Cu<sub>AX</sub> (X=1-5) particles reduced at 350°C in a 7% H<sub>2</sub> atmosphere at a) -1.6 and at b) -2.2 V vs. Ag/AgCl. Conditions: 0.1 M KHCO<sub>3</sub>, 1600 RPM, 25°C. Large spikes in current densities are caused by coverage of the working electrode surface by gas. -----55

## List of Tables

<b>Table 1</b> Examples of faradaic efficiencies (FE) for gaseous products methane (CH <sub>4</sub> ), ethylene (C <sub>2</sub> H <sub>4</sub> ), and hydrogen (H <sub>2</sub> ) for CO <sub>2</sub> or CO electroreduction, as reported for Cu of different morphologies (foils, nanofoams, reduced Cu-oxides) and supported nanoparticles, with their corresponding current densities and potentials. Values not given are listed as not reported (NR). All products were generated in 0.1M KHCO <sub>3</sub> . -----	8
<b>Table 2.</b> Solubility of CO <sub>2</sub> in various solvents at 1 atm and 25°C [25].-----	16
<b>Table 3.</b> Precursor materials and environmental conditions used for synthesis of Cu nanoparticles using the sacrificial support method. -----	23
<b>Table 4.</b> The designations for Cu nanoparticles synthesized by SSM, as distinguished by their precursor Cu content and reduction environment. -----	26
<b>Table 5.</b> BET surface areas measured for all particles with their means and standard deviations in nanometers, as calculated from SEM images of each particle. Nearly all display an approximately normal distribution, with the exception of Cu <sub>A5</sub> and Cu <sub>B5</sub> , which display multiple populations of distinct sizes (see Appendix 1).-----	27
<b>Table 6.</b> The mole percent (mol%) of Cu, CuO, and Cu <sub>2</sub> O, as determined from phase fitted XRD data for all particles synthesized using the sacrificial support method. -----	29

## 1. Introduction

Carbon dioxide (CO<sub>2</sub>), a greenhouse gas, is generated by the complete oxidation of carbon containing fuels in processes such as the burning of methane or coal that accounted for approximately 82% of the worldwide energy supply in 2014 [1]. The unregulated, continuous release of CO<sub>2</sub> by industrial scale processes since the 1850s has increased atmospheric concentrations from 278 ppm to 400 ppm [2] – quantities that strain the balance of the earth’s natural carbon cycle, leading to acidified oceans and irregular weather patterns [1,3-5]. The accumulation of CO<sub>2</sub> has been identified by climate scientists as a major contributing factor in rising global temperatures. Climate models predict drastic changes in precipitation and temperature which will impact regional and global economies, as shown in a model exploring the likelihood of a semi-permanent drought in North America (see Fig. 1) [5]. Recent discussions no longer focus

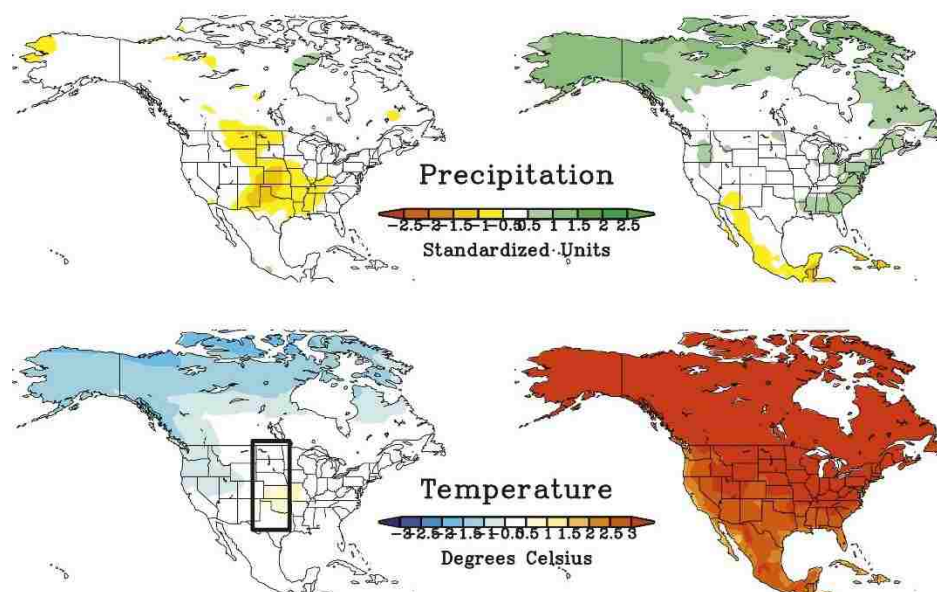


**Figure 1.** Projected changes in precipitation and temperature modeled from current atmospheric conditions without greenhouse gas reduction. On the left are trends observed from 1865-1875, on the right are predictions for 2045-2055 [5].

on *if* CO<sub>2</sub> emission rates should be decreased, but by how much and how soon they should be mitigated to avoid exceeding a global mean temperature rise of 1.5-2.0°C by 2100 [6]. The rate of CO<sub>2</sub> emission that is predicted to correspond with this limit is 44 gigatons of CO<sub>2</sub> per year (GtCO<sub>2</sub>) by 2020, which is approximately 55% of the 1991 emission rates and will require a 12 GtCO<sub>2</sub> decrease from the projected 2020 rate of 59 GtCO<sub>2</sub> (for the “no action” case) [6-7]. Consensus that CO<sub>2</sub> emissions will continue to increase necessitates that the massive scale of these ambitious emission reductions will be mitigated by the development and improvement of technological discoveries in the next few decades.

Currently, there are many possible solutions for decreasing CO<sub>2</sub> emissions; among them are increasing the percentage of energy generated from renewable or nuclear sources and utilizing CO<sub>2</sub> capture and storage (CCS) at point sources (e.g. power plants) [6, 8-9]. While CCS fundamentally prevents CO<sub>2</sub> release, it can be improved by CO<sub>2</sub> capture and conversion (CCC) into fuels or value added products (defined as chemical products or precursors that have an increased monetary value). This would simultaneously decrease the rate of emissions and possibly reintroduce CO<sub>2</sub> into the energy cycle – essentially converting carbon emitting energy sources into carbon neutral sources. This process can be implemented in batch or flow reactors, typically with low fluid quantities, and has been shown to selectively reduce CO<sub>2</sub> to specific products. One example of this is the CO<sub>2</sub> reduction to formic acid, which in optimized systems has been reported at conversion rates as high as 94.1% on lead (Pb) and between 70-80% on tin (Sn) [10]. Formic acid is used extensively in agricultural applications: as a pesticide, as an

anti-bacterial preservative, and as a food additive for feed stocks. Another example is the accomplishment of “one-pot” synthesis of syn-gas (carbon monoxide and hydrogen gas) on Ag, which requires producing the gases at a controlled molar conversion ratio of 1:2 [11-13]. Syn-gas is used in gasoline synthesis, thus having a simple method of producing this mixture is extremely desirable. A final example is the synthesis of precursors for non-steroidal anti-inflammatory drugs (NSAIDs), such as ibuprofen or naproxen, which has been reported with conversions as high as 75-80% for the electrochemical carboxylation of organic intermediates to produce acids [8]. Further, CCC could facilitate the integration of intermittent renewable energy sources (e.g., solar or wind) by storing energy for later use as reduced CO<sub>2</sub> in liquid or gas products.

In general, CO<sub>2</sub> conversion can be achieved by reduction in solid state fuel cells, on metal electrodes in aqueous solutions, or by metal complexes [9, 11]. Possible reduction products of CO<sub>2</sub> include, but are not limited to, C<sub>1</sub>-C<sub>3</sub> chained molecules such as carbon monoxide (CO), formic acid (HCOOH), methane (CH<sub>4</sub>), ethylene (C<sub>2</sub>H<sub>4</sub>), and alcohols (C<sub>x</sub>H<sub>2x+1</sub>OH) [14-28]. Solid state fuel cells are currently limited to producing CO, which is attributed to their high operating temperatures [9, 21, 29-30]. Most metal complexes that have been studied contain either platinum or palladium catalytic sites, and thus are not economically viable at their current efficiencies on the industrial scale [9]. Metal electrodes in aqueous media can be incorporated into established technologies, such as proton exchange membrane fuel cells (PEMFCs) and gas diffusion electrodes (GDEs), replacing catalysts typically employed for the hydrogen evolution reaction (HER) with catalysts designed for CO<sub>2</sub> electroreduction (CER) at the cathode



while maintaining the oxygen evolution reaction (OER), from H<sub>2</sub>O, at the anode [9,11-12, 31-32]. However, very few catalysts exhibit high current density and low applied voltage, in addition to selectivity towards a specific product and durability, which are all criteria for viable industrial application of CER on metals in aqueous media as shown in a recent survey by Jhong et al. (Fig. 2).

### 1.1 Statement of intent

Unique among metal catalysts, copper (Cu) can reduce CO<sub>2</sub> to small chained hydrocarbons and alcohols ( $\geq C_1$ ) at low temperatures and atmospheric pressures with surprisingly high conversion [24]. Since the 1980s much effort has been made to elucidate the mechanism of CO<sub>2</sub> reduction on Cu with the purpose of engineering a catalyst that will generate high hydrocarbon yields in fuel cells [20-23, 34-40]. Based on these insights, this thesis will report the results of testing the hypothesis that a porous, unsupported Cu catalyst, synthesized with the sacrificial support method (SSM) can generate stable, large current densities previously only

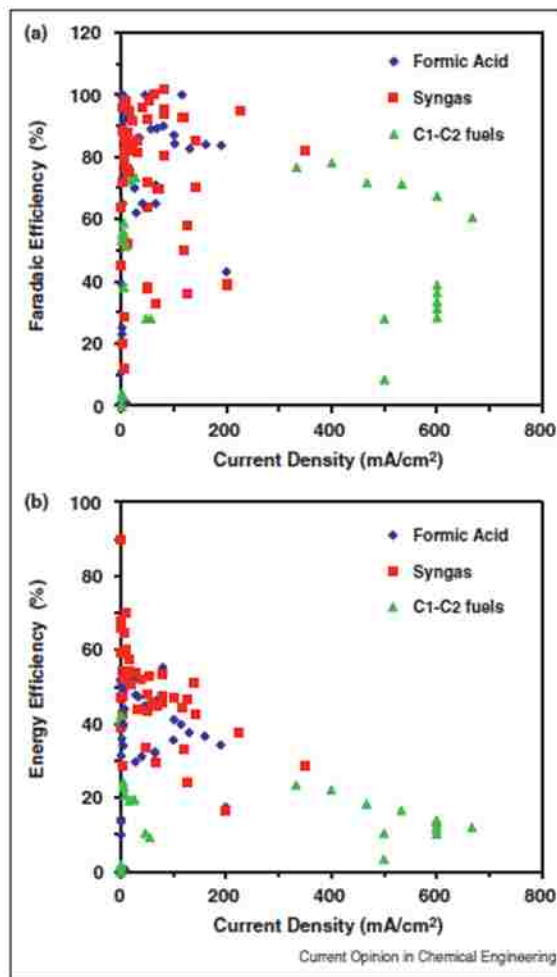


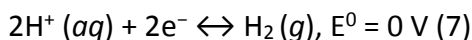
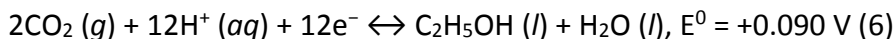
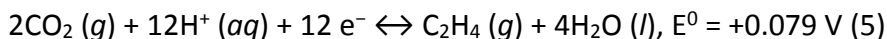
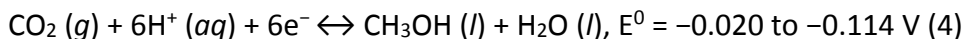
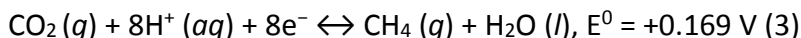
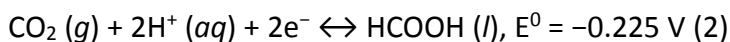
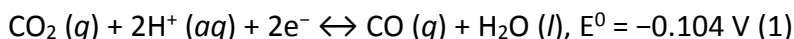
**Figure 2.** Survey of current densities (CD) of CO<sub>2</sub> reduction reported from 1985 to 2012 as compiled by Jhong et al. shows a) faradaic efficiencies (FE) towards three major products (CO, CH<sub>4</sub>, HCOOH) and b) energy efficiencies (EE), exhibiting the lack of catalysts that exhibit both high CD and high FE or EE [33].

observed for carbon supported Cu nanoparticles [41-42]. The effect of composition and morphology of the synthesized particles will be discussed in terms of electrochemical performance, with comparison to the published results of other Cu materials for CER. In probing this topic the main goals of this work are as follows: First, synthesize and characterize Cu with a porous and controllable morphology using the sacrificial support method. In doing so, determine an optimum ratio of Cu to silica in the precursor to produce a porous morphology. Second, determine if this Cu catalyst is stable when held at high potentials for periods of at least 1 hour – this criteria is essential to determine the selectivity of these materials towards a specific product in later product quantification tests. Third, determine if the SSM is a beneficial synthesis approach for CER on Cu; this will be determined on the basis of comparing current densities observed in previous studies with those of the synthesized particles.

## 2. Background

### 2.1 Carbon dioxide electroreduction on metals

CO<sub>2</sub> reduction is catalyzed on metals in aqueous solutions at 25°C, pH=6.8, V vs. the standard hydrogen electrode (SHE, Eq. 7) according to the following net reactions [10, 42]:



Where  $E^0$  is the standard equilibrium potential, defined as  $E^0 = E^0_{\text{cathode}} - E^0_{\text{anode}}$ , vs. SHE.

Metal catalysts are categorized into four primary groups, based on their primary reduction products, as observed by Hori et al.: i) HCOOH (Pb, Tl, Hg, Sn, In, Cd), ii) CO (Au, Ag, Pd, Ga, Zn), iii) CH<sub>4</sub>/C<sub>2</sub>H<sub>4</sub> (Cu), and iv) H<sub>2</sub> (Pt, Ni, Fe, Ti) [25]. These product trends have been extensively confirmed by observation in many studies and suggest different surface affinities for CO<sub>2</sub> reduction intermediates and/or dissimilar reaction mechanisms for each class of materials [14-15, 18-19, 20-23, 25, 43-45]. The catalytic activity of all metals also depends on their surface characteristics such as roughness and

surface area to volume ratios, both which affect the plane edges exposed at the surface as is typical for a surface reaction [31, 34-35, 46]. Other parameters that influence product species and the distribution of yields include the reaction potential, the system pressure and temperature, and the solution concentration and type (e.g. aqueous versus non-aqueous, solution pH, specific cation and anion species, etc.). The remainder of this chapter will focus on the specific dependencies of Cu, although to some extent, these limitations and considerations apply to all metals.

## 2.2 Carbon dioxide electroreduction on copper

### 2.2.1 Measures of merit: efficiency and selectivity

Before introducing the limiting parameters of CER in aqueous media, it is sensible to discuss the challenges of characterizing this system in which the concurrent generation of numerous, multi-phase (liquid and gas), small-chained carbon molecules requires simultaneous measurement of electrochemical performance and either/both liquid and gas phase product quantification. Electrochemical performance is measured in half-cell or fuel cell apparatuses, under potentiostatic or galvanostatic conditions, as appropriate. Liquid and gas phase products are quantified by techniques such as gas chromatography (GC), nuclear magnetic resonance analysis (NMR), or mass spectroscopy (MS) to assess the selectivity of the reaction towards a specific product. This is necessary for assignment of the fractional charge distributions of current densities generated in saturated CO<sub>2</sub> solutions, which concomitantly generates H<sub>2</sub> from aqueous solutions. Accepted measures of product selectivity and efficiency are typically expressed as energetic and faradaic efficiency, defined in Eq. 8 and Eq. 9 [34]:

$$\varepsilon_{energetic} = \sum_k \frac{E_k^0 \varepsilon_{k, Faradaic}}{E_k^0 + \eta} \quad (8)$$

where  $E_k^0$  is the standard potential of product  $k$ ,  $\varepsilon_{k, Faradaic}$  is the Faradaic efficiency (FE) of product  $k$ , and  $\eta$  is the cell overpotential (Eq. 10, below).

$$\varepsilon_{Faradic} = \frac{z \cdot n \cdot F}{Q} \quad (9)$$

where  $z$  is the number of electrons exchanged (e.g.  $z = 2$  for reduction of  $\text{CO}_2$  to  $\text{CO}$ ),  $n$  is the stoichiometric number of moles for a given product,  $F$  is Faraday's constant (96,485 C mol<sup>-1</sup>), and  $Q$  (C) is the charge passed. Faradaic efficiencies of CER towards hydrocarbons on Cu range from < 3-79% (see Table 1). In many of the discussions that follow, only partial quantification of products (one phase is quantified) are reported in published literature. However, in most cases the materials exhibit high total faradaic efficiency (nearing 100%), indicating that the quantity of products in the excluded phase

**Table 1** Examples of faradaic efficiencies (FE) for gaseous products methane ( $\text{CH}_4$ ), ethylene ( $\text{C}_2\text{H}_4$ ), and hydrogen ( $\text{H}_2$ ) for  $\text{CO}_2$  or  $\text{CO}$  electroreduction, as reported for Cu of different morphologies (foils, nanofoams, reduced Cu-oxides) and supported nanoparticles, with their corresponding current densities and potentials. Values not given are listed as not reported (NR). All products were generated in 0.1M  $\text{KHCO}_3$ .

Material (Catalyst/ Reactant)	Potential (vs. SHE)	Current Density (mA cm <sup>-2</sup> )	Total Hydro- carbon FE	CH <sub>4</sub> FE	C <sub>2</sub> H <sub>4</sub> FE	H <sub>2</sub> FE
Cu / CO <sub>2</sub> [25]	-1.44 V	5	78.8	33.3	25.5	20.5
Cu / CO [25]	-1.40 V	2.5	37.5	16.3	21.2	45.5
Cu / CO <sub>2</sub> [25]	-1.41 V	5	59.1	29.4	30.1	10.9
Cu / CO <sub>2</sub> [25]	-1.39 V	5	62.3	32	30.3	14.5
Cu from Cu <sub>2</sub> O / CO <sub>2</sub> [47]	-1.50 V	NR	35-40	NR	NR	NR
Cu nanofoams / CO <sub>2</sub> [48]	-1.50 V	8	< 3.0	1.3	1.4	60.0
20 wt% Cu nanoparticles on C / CO <sub>2</sub> [42]	-1.60 V	3	ca. 50	ca. 25	ca. 25	ca. 25

is a very small amount and does not diminish the value of these analyses.

### 2.2.2 Overpotential and the mechanism of carbon dioxide electroreduction

A significant challenge to the application of CO<sub>2</sub> electroreduction in a PEM-type cell is the large overpotential exhibited by the reaction ( $\eta$ , defined by Eq. 10), which is typically in the range of approximately 1.0 Volt [49, 25]:

$$\eta = E_{\text{theoretical}} - E_{\text{observed}} \quad (10)$$

where  $E_{\text{theoretical}}$  is the thermodynamically predicted reaction potential and  $E_{\text{observed}}$  is the experimentally measured reaction potential. While it is generally accepted that the large overpotential of CER is due to a slow and inefficient kinetics, determining which intermediate step in the reaction mechanism is rate limiting for such a complex system is extremely difficult [22, 38-39, 50-51]. Beyond signifying a much higher energy cost than is thermo-dynamically predicted, this  $\eta$  shifts the reaction potential of CO<sub>2</sub> reduction into the region where H<sub>2</sub> evolution is theoretically possible, at -0.03 V vs. the reference hydrogen electrode (RHE) [10], defined by Eq. 11:

$$E_{\text{RHE}} = E^0 - 0.059 \times pH \quad (11)$$

where  $E^0$  is the standard hydrogen potential (Eq. 7), and  $pH$  is measured from the bulk electrolyte [49]. The dependence of product efficiencies on applied potential was observed by Hori et al., with less negative potentials predominantly generating H<sub>2</sub> and more negative potentials generating a range of products (Fig. 3) [22]. The source of this change in product distribution was illuminated by Peterson et al. who calculated that H<sub>2</sub> formation is likely the first open reaction pathway on Cu, but is limited by the formation

of surface oxides on Cu in aqueous solutions and at potentials more positive than -0.40 V vs. RHE [39]. Although adsorbed atomic hydrogen ( $H_{ad}$ ) is a surface species that participates in  $CO_2$  reduction, it is hypothesized that HER occurs at a faster rate, and at less negative potentials, so the competitive occupation of active sites by adsorbed  $CO_2$  is slow and limits the availability of adsorbed CO intermediates ( $CO_{ad}$ ) at these potentials [22, 38-39]. Beyond

potentials of ca. -1.2 V vs. SHE there are several different reaction pathways that are energetically possible, as evident by

the simultaneous appearance of CO,  $CH_4$ ,  $C_2H_4$ , and  $HCOOH$  – all seemingly sharing a rate limiting step that Jordan and Smith proposed is the ionization of  $CO_2$  to its anion radical ( $CO_2^{\cdot-}$ ) which could either be in solution or weakly adsorbed to Cu [52]. Hori et al. elaborated on this hypothesis, proposing that  $CO_2^{\cdot-}$  was reduced and adsorbed as CO (Eq. 12), and subsequently further reduced and hydrogenated to form one of two carbonyl forms: either adsorbed COH ( $COH_{ad}$ ) or CHO ( $CHO_{ad}$ ).

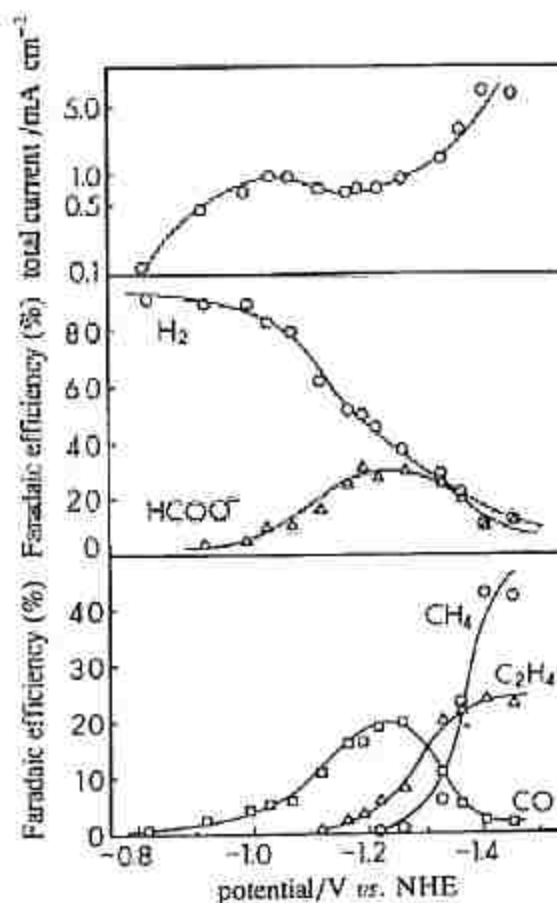
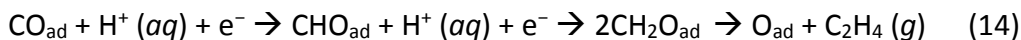
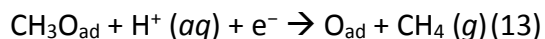
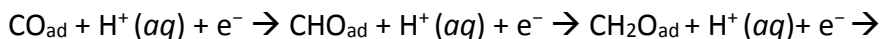


**Figure 3.** A graph depicting the range of products and their faradaic efficiencies for  $CO_2$  reduction on Cu as a function of potential, generated and reported by Hori et al. Total faradaic efficiency is depicted in the top segment [22].

The adsorption, reduction, and subsequent hydrogenation of  $\text{CO}_2^-$ , observed via *in-situ* Fourier transfer spectroscopy (FTIR) on other metal electrodes, was thought to be stabilized by the d-orbitals of transition metals in a side-on or C-on orientation with the active site, similar to the electronic configuration of adsorbed  $\text{CO}_2$ , although this is not a universally accepted step in the reaction pathway [22]. Additional studies experimentally demonstrated that  $\text{HCOO}^-$  is not further reduced on Cu while CO is, confirming that  $\text{CO}_{\text{ad}}$  is the intermediate in the  $\text{CO}_2$  reduction mechanism [22]. Peterson et al. calculated the free energies for possible reaction intermediates using a computational hydrogen electrode (CHE) model coupled with density functional theory (DFT) adsorption energies to confirm that an adsorbed CHO intermediate is likely in the intermediate species in the pathway to both  $\text{CH}_4$  and  $\text{C}_2\text{H}_4$ , shown in Eq. 13-14 [38]:



After the formation of adsorbed CO ( $\text{CO}_{\text{ad}}$ ) at potentials less than -0.41 V vs. RHE, the additional reduction to  $\text{CHO}_{\text{ad}}$  was calculated as energetically favorable at potentials greater than -0.74 V vs. RHE. The potentials at which  $\text{H}_2$  and  $\text{CO}_{\text{ad}}$  are possible energetic pathways for CER are nearly identical (-0.40 and -0.41 V vs. RHE, respectively), but clearly the further reduction of  $\text{CO}_{\text{ad}}$  has a larger energy barrier and thus explains the preferential formation of  $\text{H}_2$  at less negative potentials. Although these studies are useful as a basis for understanding a possible mechanism of CER on Cu, they are less



predictive for Cu alloys or for Cu particles distributed on carbon supports because the electronic and surface properties of active sites are altered enough to change adsorption energies of intermediate species [39].

### 2.2.3 Influence of copper surface structure on selectivity

Studies on the effect of single and poly-crystalline Cu have revealed that CER faradaic yields are very sensitive to surface structure. Hori et al. show that  $C_2H_4$  is produced in larger quantities on Cu (110), while  $CH_4$  is the favored product on Cu (111), when compared with the products generated at the same potentials on Cu foil [34-35]. Higher index facets, such as Cu (311), Cu (511), and Cu (711) were shown to produce higher quantities of  $C_2H_4$ , in addition to a mixture of longer chained aldehydes, ketones, acids, and alcohols ( $\geq C_2$ ). As discussed by Baturina et al., these differences predict the change in product distributions due to morphology as seen in several studies on Cu surfaces developed with different techniques [42]. Electrodeposited 3-dimensional foams of varying thickness produced  $C_2H_4$  at a faradaic efficiency of 13%, while Cu mesh produced more  $CH_4$  than  $C_2H_4$  (ca. 12% and 8%, respectively) [53]. Further, Baturina et al. suggest that because nanoparticles of Cu are comprised of low-coordination sites and low-index facets (edges, defects, and corners), and would be expected to generate mostly  $C_2$  products in CER because of the similarity of these sites to Cu (311), Cu (511), and Cu (711). This is supported by the observations of Tang et al. that Cu particles of 50-100 nm produced primarily  $C_2H_4$  and little  $CH_4$  (faradaic efficiencies of ca. 37% and 1%, respectively) [54]. Sen et al. studied hierarchal structured Cu nano-foams and observed a +200 mV improvement for the onset of CER (detection of products), and an increase in

faradaic efficiency towards HCOOH, which they attribute to an increased ratio of Cu (111) : Cu (200) in the material [48]. These examples suggest that product distributions of hydrocarbons can be controlled by developing Cu morphologies with specific product affinities.

#### 2.2.4 Modifications to copper: influence of alloying and conductive supports

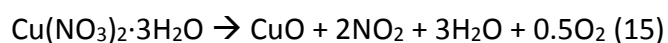
As previously stated, predicting the performance and selectivity of alloys or carbon supported Cu materials is difficult from a theoretical vantage. Peterson and Norskov conclude their discussion of possible CER mechanisms with recommendations for improvements of CER, such as alloying Cu with an element having a higher oxygen affinity to increase the stability of CER CO intermediates [39]. In an early study, Wanatabe et al. observed differences in CER onset and product distribution (CO, HCOOH, and CH<sub>3</sub>OH) of CER when alloying Cu with Ni, Sn, Zn, Pb, Cd and Ag [55]. They observed that the  $\eta$  was decreased in all cases; CO production increased for Cu alloyed with Zn, Cd, or Ag, while HCOOH production was increased for Cu alloyed with Sn or Pb, and CH<sub>3</sub>OH (rarely produced in measurable quantities) was generated on Cu alloyed with Cd or Ni. In a recent study, Kim et al. synthesized bimetallic gold and copper (Au-Cu) nanoparticles, observing that increasing the atomic ratios of Au : Cu increases CO faradaic yields, decreases hydrocarbon production while simultaneously suppressing H<sub>2</sub> generation, and conclude that tuning the electronic affinities of intermediate CER surface species is possible and also dependent on the relative geometric positioning of elements [56]. Baturina et al. observed the effects of Cu nanoparticles (10-30 nm) on the selectivity of CER towards hydrocarbons on various carbon supports. Increased

selectivity towards  $\text{CH}_4$  at  $-1.4$  V vs. SHE is attributed to carbon induced HER spillover at potentials greater than  $-1.0$  V vs. SHE. Well dispersed nanoparticles (12-19 nm diameter) displayed a lower  $\eta$  (+200 mV) for  $\text{C}_2\text{H}_4$  production, suggesting increased activity towards this species that may be resultant from the increased low-coordination sites of these particles [42]. Hossain et al. varied the weight percent of Cu nanoparticles loaded on carbon nanotubes (CNTs), reporting an optimum value of 20wt% with a  $\text{CH}_3\text{OH}$  faradaic efficiency of ca. 35%, but it is impossible to determine the effect on relative efficiencies of  $\text{H}_2$  and hydrocarbons because they failed to report gas phase quantification and the total faradaic efficiency [57]. With the above examples of possible Cu surface variations, it can be understood that the surface sensitivity of CER, extends to alloys and carbon supports, and requires the development of well-controlled synthesis methods to produce surfaces of specific geometric and compositional parameters.

### 2.3 Copper nanoparticles: challenges in material synthesis

The synthesis of Cu nanoparticles is challenging because of the tendency of Cu to oxidize to cupric oxide ( $\text{CuO}$ ,  $\text{Cu}^{2+}$ ) and cuprous oxide ( $\text{Cu}_2\text{O}$ ,  $\text{Cu}^+$ ), both which spontaneously form at room temperatures in the presence of air and minimal moisture [58]. Methods for successful synthesis of Cu nanoparticles ranging in size from 15 to 100 nm implement thermal reduction and chemical reduction with many different types of solvents [42, 59-60]. It is difficult to make these sized particles without oxidation, further it is difficult to control the degree and type of oxidation that occurs, which explains the distinct lack of Cu nanoparticles of varied morphologies in nanoparticles. As

a result, most patterned structures are typically grown electrochemically on flat surfaces, as in the case of honey-comb and 3-D structures, just discussed [48, 53]. The thermal decomposition of a common precursor, Cupric nitratetrihydrate ( $\text{Cu}(\text{NO}_3)_2 \cdot 3\text{H}_2\text{O}$ ), has been extensively studied and shown to generate multiple nitrogen and oxygen containing gas phase products upon decomposition (between 150°C and 225°C) [61]. L'vov et al. propose that decomposition of  $\text{Cu}(\text{NO}_3)_2 \cdot 3\text{H}_2\text{O}$  occurs in three stages: i) "deaquation" up to 127°C ii) incomplete thermal decomposition by gasification mechanism at 187°C with the formation of  $\text{Cu}_2(\text{OH})_3\text{NO}_3$  iii) further decomposition to CuO at 257°C (Eq. 15) [62-63]:



Additionally, L'vov et al. postulated that the reduction of nitrogen dioxide ( $\text{NO}_2$ ) is catalyzed on CuO, resulting in the formation of nitric oxide (NO) according to the following reaction (Eq. 16) [62]:



Ryu et al. observed a similar intermediate ( $\text{Cu}_2(\text{OH})_3\text{NO}_3$ ) in their study of the thermal decomposition of  $\text{Cu}(\text{NO}_3)_2 \cdot 3\text{H}_2\text{O}$  on activated carbon fibers, where they observed the formation of CuO at 200°C, CuO/ $\text{Cu}_2\text{O}$  between 230°C and 255°C, and  $\text{Cu}_2\text{O}$ /Cu between 300°C and 350°C [64]. Both Ryu et al. and L'vov et al. note that the thermal decomposition  $\text{Cu}(\text{NO}_3)_2$  begins within the temperature range where dehydration may be incomplete, thus water is present in small amounts in the reactive phase of this decomposition and makes it difficult to control the amount, extent and type of oxide

formation, even in a reductive environment [62, 64]. Further, at temperatures greater than 350°C, Cu readily sinters and nanoparticles formed begin to aggregate into larger particles.

## 2.4 Electrolyte

### 2.4.1 The limited solubility of carbon dioxide in solution and the effect of pressure

Beyond catalyst considerations, CER is limited by the low solubility of CO<sub>2</sub> in both aqueous and non-aqueous solutions, which restricts the reactant concentration at atmospheric pressure (see Table 2) [22, 43, 53]. While increasing CO<sub>2</sub> pressure to increase its solubility may seem a straight-forward response to this limitation, it has been shown that Cu selectivity shifts towards CO and HCOOH and away from hydrocarbons with changes in pressure. Hara et al. demonstrated that hydrocarbon selectivity decreases from 60% to 15% with an increase in pressure from 1 atm to 30 atm. They posit that pressure controls CO<sub>2</sub> flux at the electrode surface; shifts in product distribution occurs when the current applied during galvanostatic experiments exceeds an optimum CO<sub>2</sub> flux, resulting in a shift in adsorbed species and altering the reaction pathway [45].

**Table 2.** Solubility of CO<sub>2</sub> in various solvents at 1 atm and 25°C [25].

Solvent	Concentration (M)
Aqueous media	0.033
Tetrahydrofuran (THF)	0.205 ± 0.008
Acetonitrile (AN)	0.279 ± 0.008
Dimethylformamide (DMF)	0.199 ± 0.006
Dimethylsulphoxide (DMSO)	0.138 ± 0.003

This hypothesis is supported by other studies which demonstrate a shift in selectivity away from hydrocarbons at atmospheric pressures beyond some limiting current density [44, 67-70]. Clearly, CO<sub>2</sub> pressure influences CER products, but it would best be optimized at some later stage, after a catalyst has been shown to perform at atmospheric pressure and there is a general understanding of the reaction mechanism. Other alternatives to solubility limitations include using aprotic solutions, but this restricts possible products to CO due to the absence of protons, and are not useful in discussion of CER to hydrocarbons [25]. As a final comment on pressure, the decrease of solubility at very low or high temperatures should be considered, where the concentration dependence of a gas dissolved in solution can be approximated by Eq. 17:

$$p = k_H(T) \times c \quad (17)$$

where  $p$  (atm) is the partial pressure of the gas above the solution,  $c$  (mol L<sup>-1</sup>) is the concentration of the gas in solution, and  $k_H$  (mol-atm L<sup>-1</sup>) is Henry's constant, which is not truly a constant because of its functional dependence on temperature [71]. There are very few studies that maintain constant pressure for temperature changes.

#### 2.4.2 The effect of solution pH

In addition to solution type sensitivity, the product distribution of CER is influenced by the pH of aqueous solutions and can vary widely depending on the bulk pH of the solution [22]. Potassium bicarbonate (KHCO<sub>3</sub>) is frequently used as the solution in CER because the potassium cation (K<sup>+</sup>) has the highest faradaic selectivity towards C<sub>2</sub>H<sub>4</sub> (14%) and CH<sub>4</sub> (16%), with the lowest selectivity towards H<sub>2</sub> [47]. Hori et

al. probed the effect of varying  $\text{KHCO}_3$  from 0.03 to 1.5 M (Fig. 4), observing that faradaic yields of hydrocarbons drop off after 0.5 M, with the highest yield of  $\text{C}_2\text{H}_4$  at low  $\text{KHCO}_3$  concentrations, suggesting that selectivity is shifted because of changes in local pH [22]. Gupta et al. confirmed this suggestion with their mathematical model of the surface pH as a function of bulk pH concentration for  $\text{KHCO}_3$  solutions. Calculations predicted that the pH near the boundary layer more closely resembled the bulk pH for higher

$\text{KHCO}_3$  concentrations, with large pH differences for lower concentrations (e.g. bulk pH = 6.8, local pH = 9.8 for 0.1 M  $\text{KHCO}_3$  with a boundary layer thickness of 0.01 cm) [43].

Until now, these pH data have been used to explore possible mechanistic pathways, but they will be important considerations for later applications in fuel cells.

Another possible effect of high pH solutions is the destabilization of metallic Cu, which can decrease activity by reducing Cu catalytic sites. Metallic Cu can traverse regions of instability, as shown in the Pourbaix diagram for Cu (Fig. 5) [72], in the range of potentials and in low solution concentrations (<0.1 M), where pH gradients near the surface can vary substantially (as in 0.1 M  $\text{KHCO}_3$  which is modeled as having a surface

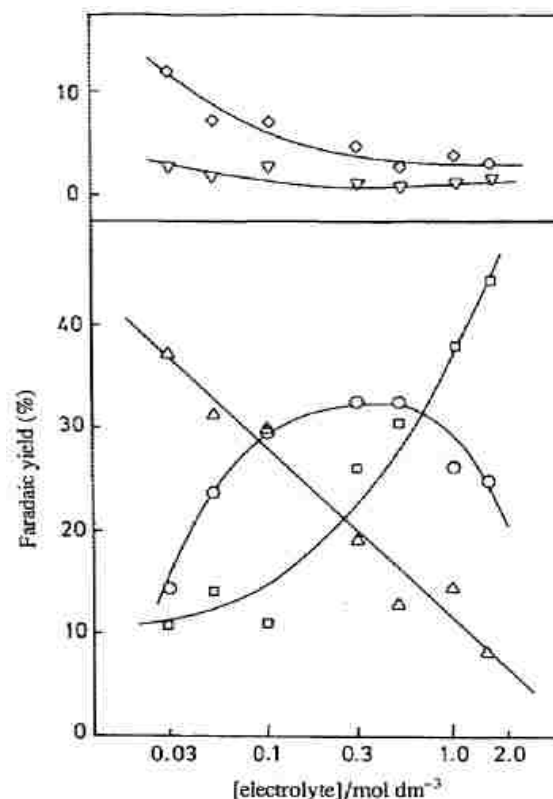


**Figure 4.** The effect of pH on product distribution for  $\text{KHCO}_3$  solutions varied from 0.03 to 1.5M where:  $\square$  - $\text{H}_2$ ,  $\Delta$  - $\text{C}_2\text{H}_4$ ,  $\diamond$  - $\text{C}_2\text{H}_5\text{OH}$ ,  $\circ$  - $\text{CH}_4$ ,  $\Delta^{-1}$  -  $\text{C}_3\text{H}_7\text{OH}$  [22].

pH of 9.8 and a bulk concentration of 6.8 under saturated  $\text{CO}_2$  conditions for highly active surfaces) [10-11, 42]. However, this effect can also be exploited: Kas et al. electrochemical reduced thin films of  $\text{Cu}_2\text{O}$  to Cu at neutral pH at potentials greater than -0.3 V vs. RHE, essentially exposing plane-indices and edges associated with reduced  $\text{C}_2\text{O}$ , and increasing selectivity towards  $\text{CH}_3\text{OH}$  [47].

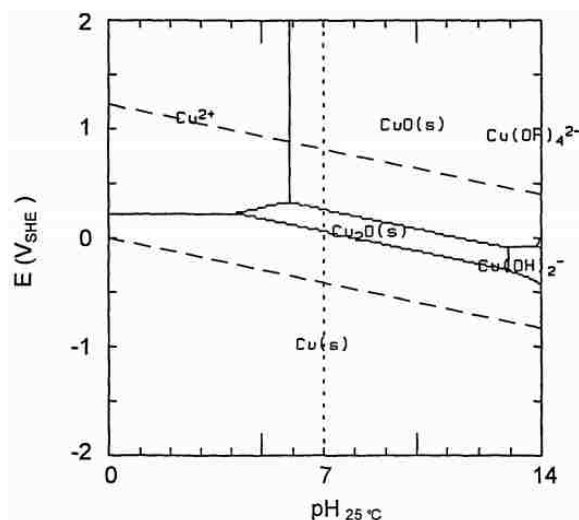


**Figure 5.** The Pourbaix diagram for Cu in aqueous solutions; note the phase boundary between Cu and  $\text{Cu}_2\text{O}$  exists near 0 V vs. SHE at pHs 9-10 [72].

#### 2.4.3 Deactivation of copper by trace metals

A final consideration of Cu in aqueous solutions is its observed sensitivity to the poisoning of its active catalytic surface sites by very low quantities of Fe and Zn over time. These trace elements are present in even very high purity salts used for solutions,  $\leq 5$  ppm in materials  $\geq 99.95\%$  purity [66]. Pre-electrolysis of solutions used as an electrolyte is one method developed to remove these trace amounts of metals, but it would be more convenient for large scale applications to either develop a more robust catalyst or to incorporate another material that would filter out these trace amounts from solutions used in electrolysis [24].

#### 2.5 Temperature

Increasing the temperature of electrolysis for CER has been shown to increase overall efficiency (i.e., higher current density), while decreasing selectivity towards



hydrocarbons. Hori et al. showed that increasing the temperature of reaction from 0°C to 40°C decreases the hydrocarbon selectivity from ca. 62% to 5%, respectively [20]. These conditions also resulted an increase in the faradaic efficiency of C<sub>2</sub>H<sub>4</sub> from ca. 0% to 20%. Wanatabe et al. describe an optimum reaction condition for CER at a temperature of 0°C [73]. As briefly mentioned earlier, either extremely high or low temperatures can decrease the concentration of CO<sub>2</sub> in solution by altering its solubility – an effect that convolutes extracting kinetic parameters for CO<sub>2</sub> conversion towards any of its possible products. It is worth noting that most studies of high temperature CER (albeit on other metals) have shown high faradaic yields for CO and H<sub>2</sub>, even when combined with high pressures [9, 21, 73]. Until the mechanism of multi-product reduction at room temperature and atmospheric pressure is well understood, it is unlikely that temperature dependent kinetic parameters will be forthcoming.

## 2.6 Further considerations for integration into application

Discussion thus far has focused on distinguishing important variables of CER on Cu to contextualize the complexity of this system. Despite all these challenges, Cu is still an attractive catalyst because it generates hydrocarbons with high faradaic yields at mild conditions, at atmospheric pressure and temperatures between 18.5°C and 25.0°C [20-23, 34]. If Cu is to be employed in PEM-type fuel cells as an approach to decrease CO<sub>2</sub> emissions, as suggested earlier, it will need to be optimized for high conductivity, low mass transport limitations, low  $\eta$ , fast kinetics, with long-term stability, preferably using low cost materials and synthesis methods. Material synthesis techniques that have typically been used to improve these characteristics for PEMFC catalysts include

dispersion of nanoparticles on carbon supports (increased activity, conductivity, and mass transport) and alloying elements as nanoparticles (decreased cost, increased activity and conductivity). As outlined above, many of these methods have been employed to develop Cu as a CER catalyst, with some varied results. This distinguishes a major setback to understanding the feasibility of Cu for fuel cells applications: there are no comprehensive studies into the statistical significance of variables known to influence CER total and product faradaic efficiencies. Current methodology separates catalyst characterization into two primary approaches: 1) electrochemical characterization of catalysts as thin films in a kinetically limited regime under potentiostatic or galvanostatic conditions, as in rotating disk electrodes and 2) electrochemical characterization of membrane electrode assembly cells (MEA), where more realistic diffusion limitations can be resolved under galvanostatic conditions. Major failings of each include: 1) studies cannot model and predict possible changes in mechanism in the expansion of thin film to 3-dimensional structure 2) studies rarely include deconvolution of  $E_{\text{cathode}}$  from the total cell potential and do not deviate from standard procedures to determine the effect of supports and ionomers on the cell. Although both characterization approaches provide valuable insight into catalyst performance, at present there is no way to reconcile the two into a unified body of data about the general system, essentially these failings make it impossible to compare the results of MEA and half-cell studies, which will be especially important for a system as sensitive as Cu for CER [33]. With this in mind, the purpose of this thesis is to probe the effect of morphology on CER product distribution, in other words it is an exploration

into the kinetics of this system, with the understanding that this is a partial qualification of its suitability for application.

### 3. Experimental Methods

#### 3.2 Synthesis of Cu nanoparticles

Cu nanoparticles were synthesized using the sacrificial support method, a method developed by UNM [74-83]. The weight percent (wt%) of Cu to fumed silica was varied from 5-40wt% and calculated for 500 mg batches. For each ratio the calculated amount of Cupric nitratetrihydrate ( $\text{Cu}(\text{NO}_3)_2 \cdot 3\text{H}_2\text{O}$ , 98.0-103%, Sigma-Aldrich) was dissolved in 10 mL ultrapure deionized water (DI  $\text{H}_2\text{O}$ , Millipore, 18.2  $\text{M}\Omega$  cm). The corresponding amount of fumed silica (Carb-O-Sil ©, EH-5, 380  $\text{m}^2 \text{g}^{-1}$ ) was whetted with DI  $\text{H}_2\text{O}$  and dispersed by ultrasonic force (Tekmar Sonic Disruptor). The  $\text{Cu}(\text{NO}_3)_2 \cdot 3\text{H}_2\text{O}$  solution was combined and dispersed in the colloidal silica suspension by ultrasonic force. The resultant solution was stored at 85°C until completely dry (12-24 hours) and ground into a fine powder with an agate mortar and pestle. The final weight of the powder was recorded and divided into two parts for thermal reduction. Each half was reduced for 2 hours at the following conditions: i) at 350°C in a 7%  $\text{H}_2$  (7%  $\text{H}_2$ , 93%  $\text{N}_2$ , Argyle) atmosphere ii) at 250°C in a 100%  $\text{H}_2$  (Matheson Tri-gas) atmosphere. Table 3 summarizes the Cu to silica ratios, reduction environments, and reduction temperatures used.

**Table 3.** Precursor materials and environmental conditions used for synthesis of Cu nanoparticles using the sacrificial support method.

Precursor weight percent ratios of Cu : EH-5					Atmosphere	Temperature (°C)
5 : 95	10 : 90	20 : 80	30 : 70	40 : 60	7% $\text{H}_2$ , 93% $\text{N}_2$	350
5 : 95	10 : 90	20 : 80	30 : 70	40 : 60	100% $\text{H}_2$	250

Once cooled, the powders were sealed by Parafilm® in their respective environments and allowed to equilibrate with an oxygen containing environment (air) for one week. The reduced powders were combined and etched for 12 hours with 25 mL 7M potassium hydroxide (KOH) prepared from DI H<sub>2</sub>O and KOH pellets (≥85%, EMD). The nanoparticles were separated from solution using centrifugal force (Labnet Hermle Z400) and rinsed with DI H<sub>2</sub>O until pH= 7.

### 3.3 Characterization

#### 3.3.1 Material characterization

The specific surface area of the catalysts was measured using Brunauer-Emmett-Teller measurements (BET, Micrometrics Gemini BET Analyzer). The physical morphology of the catalysts was observed by imaging using scanning electron microscopy (SEM, Hitachi S-5200). The bulk composition of the catalysts was determined using X-ray diffraction (XRD, Scintag Pad V, Cu anode).

#### 3.3.2 Electrochemical characterization

The electrochemical activities of the catalysts were characterized by rotating disk electrode method (RDE, Pine Wavedriver and Pine Biopotentiostat AFCBP1) in a 0.1M KHCO<sub>3</sub> solution (pH=6.8) prepared from deionized water and granular KHCO<sub>3</sub> (99.7-100.5%, Macron Chemicals). Inks were prepared from 2.0 mg of catalyst dispersed in a solution of 0.30 mL 0.5wt% ionomer (5wt%, Nafion™), 0.74 mL isopropyl alcohol (≥99.7%, Sigma Aldrich), and 2.96 mL DI H<sub>2</sub>O (final concentration: 0.5 mg mL<sup>-1</sup>). Inks were deposited at a loading of 20 μg cm<sup>-2</sup> on a glass carbon electrode (surface areas: 0.196 cm<sup>2</sup> and 0.2475 cm<sup>2</sup>, Pine Instruments) and dried in air at room temperature. All

electrochemical experiments were performed with 100 mL CO<sub>2</sub> (99.5%, Argyle) or N<sub>2</sub> (Argyle) saturated solution in a standard five neck electrochemical cell (200 mL, Pine Instruments) at 25°C using a Pt wire counter-electrode and a Ag/AgCl reference electrode (saturated KCl solution, +0.197 V vs. SHE, Radiometer Analyticals). Prior to all experiments the working electrode was stabilized by cyclic voltammetry at 100 mV s<sup>-1</sup>. Cyclic voltammetry was performed at a scan rate of 20 mV s<sup>-1</sup> at 1600 rotations per minute (RPM) between 0.6 and -2.0 V vs. Ag/AgCl. Cyclic voltammetry was also performed at scan rate of 1 mV s<sup>-1</sup> without rotation between 0.6 and -2.0 V vs. Ag/AgCl. Bulk electrolysis was performed at -1.2, -1.6 and -2.2 V vs. Ag/AgCl for 1 hour with and without rotation (1600 RPM, 0 RPM respectively).

## 4. Results and Discussion

A series of catalysts were prepared using the sacrificial support method (SSM) by varying the precursor wt% of Cu to silica and the reduction environment with the intent of producing porous Cu nanoparticles. The designations to identify these Cu nanoparticles according to their synthesis conditions are listed in Table 4. The criteria for successful implementation of this synthesis method for producing Cu nanoparticles includes an open, sponge-like morphology, a relatively high BET surface area, high Cu<sup>0</sup> content/low oxide content, and exhibited stable electrochemical activity with current densities between or greater than 0.5 to 20 mA cm<sup>-2</sup> within the potential range of CER (-1.0 to -2.2 V vs. Ag/AgCl) [10, 33].

### 4.1 Characterization

#### 4.1.1 Scanning electron microscopy

The morphology of the catalysts was confirmed by SEM (Fig. 6-7). The mean and standard deviation of these particle widths are reported in Table 5 (for details refer to Appendix 1). Widths measured are the chords of non-spherical and the diameters of

**Table 4.** The designations for Cu nanoparticles synthesized by SSM, as distinguished by their precursor Cu content and reduction environment.

Weight % Cu : EH-5 in precursor	7% H <sub>2</sub> atmosphere 350 °C	100% H <sub>2</sub> atmosphere 250 °C
5 : 95	Cu <sub>A1</sub>	Cu <sub>B1</sub>
10 : 90	Cu <sub>A2</sub>	Cu <sub>B2</sub>
20 : 80	Cu <sub>A3</sub>	Cu <sub>B3</sub>
30 : 70	Cu <sub>A4</sub>	Cu <sub>B4</sub>
40 : 60	Cu <sub>A5</sub>	Cu <sub>B5</sub>

spherical particles. The  $\text{Cu}_{\text{A}1}$  and  $\text{Cu}_{\text{A}2}$  particles (Fig. 6a-6b) exhibit morphology typical of the SSM, with voids from the etched silica clearly visible. The size of these voids correspond to the particle radius range reported for EH-5 [82]. The particles made from  $\text{Cu}_{\text{A}3}$ ,  $\text{Cu}_{\text{A}4}$ , and  $\text{Cu}_{\text{A}5}$  fail to exhibit this morphology (Fig. 6c-6e); additionally, these particles are larger and exhibit more varied particle shapes, such as hexagonal (Fig. 6d) and rectangular shapes (Fig. 6c), and shard-like structures (Fig. 6e). The  $\text{Cu}_{\text{B}1}$ ,  $\text{Cu}_{\text{B}2}$ , and  $\text{Cu}_{\text{B}3}$  particles exhibit morphology typical of SSM (Figs. 7a-7c). The  $\text{Cu}_{\text{B}4}$  particles exhibit some variance of shape (Fig. 7d), and maintain some of the connective, void shaped morphology. The  $\text{Cu}_{\text{B}5}$  particles do not exhibit the sponge-like, void shaped morphology (Fig. 7e), and similar to the  $\text{Cu}_{\text{B}4}$  and  $\text{Cu}_{\text{B}5}$  particles (Fig. 6d-6e) are quite varied in shape and size. The consistency of morphology and shape visible for most of the  $\text{Cu}_{\text{B}x}$  ( $x=1-5$ ) particles can be attributed to temperature effects – the  $\text{Cu}_{\text{A}x}$  ( $x=1-5$ ) particles are produced at temperatures where sintering may begin to occur (350 °C) and the surface energy of small particles are thermodynamically unfavorable, thus the SSM morphology may be destroyed by larger particles forming from small near neighbors [61]. In both the

**Table 5.** BET surface areas measured for all particles with their means and standard deviations in nanometers, as calculated from SEM images of each particle. Nearly all display an approximately normal distribution, with the exception of  $\text{Cu}_{\text{A}5}$  and  $\text{Cu}_{\text{B}5}$ , which display multiple populations of distinct sizes (see Appendix 1).

Sample (x)	$\text{Cu}_{\text{A}x}$			$\text{Cu}_{\text{B}x}$		
	Width (nm)	$\sigma$ (nm)	BET Surface Area ( $\text{m}^2 \text{g}^{-1}$ )	Width (nm)	$\sigma$ (nm)	BET Surface Area ( $\text{m}^2 \text{g}^{-1}$ )
1	29.8	9.4	20.0	21.5	6.7	25.1
2	60.5	21.5	10.4	29.3	11.3	20.8
3	82.7	34.4	6.0	48.1	20.9	11.1
4	78.3	35.0	3.8	48.6	19.9	11.8
5	60.0	30.2	3.4	78.8	33.6	7.0



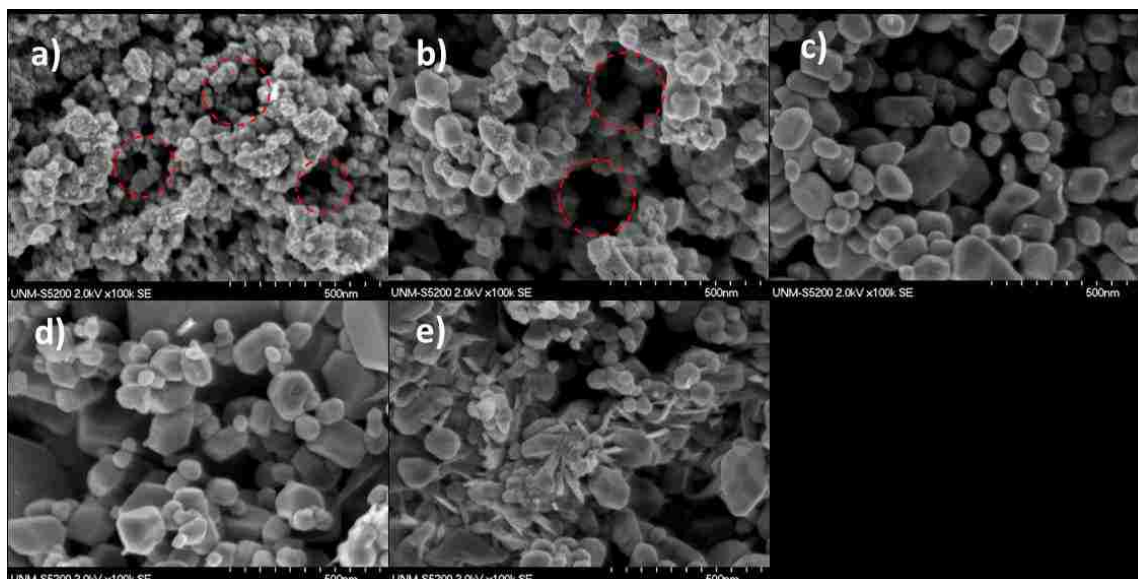


**Figure 6.** SEM images of Cu nanoparticles synthesized at 350 °C in a 7% H<sub>2</sub> reduction atmosphere: a) Cu<sub>A1</sub>, b) Cu<sub>A2</sub>, c) Cu<sub>A3</sub>, d) Cu<sub>A4</sub>, and e) Cu<sub>A5</sub>. The Cu<sub>A1</sub> & Cu<sub>A2</sub> particles (a-b) exhibit sponge-like morphology consistent with the sacrificial support method (voids from EH-5 indicated in red).

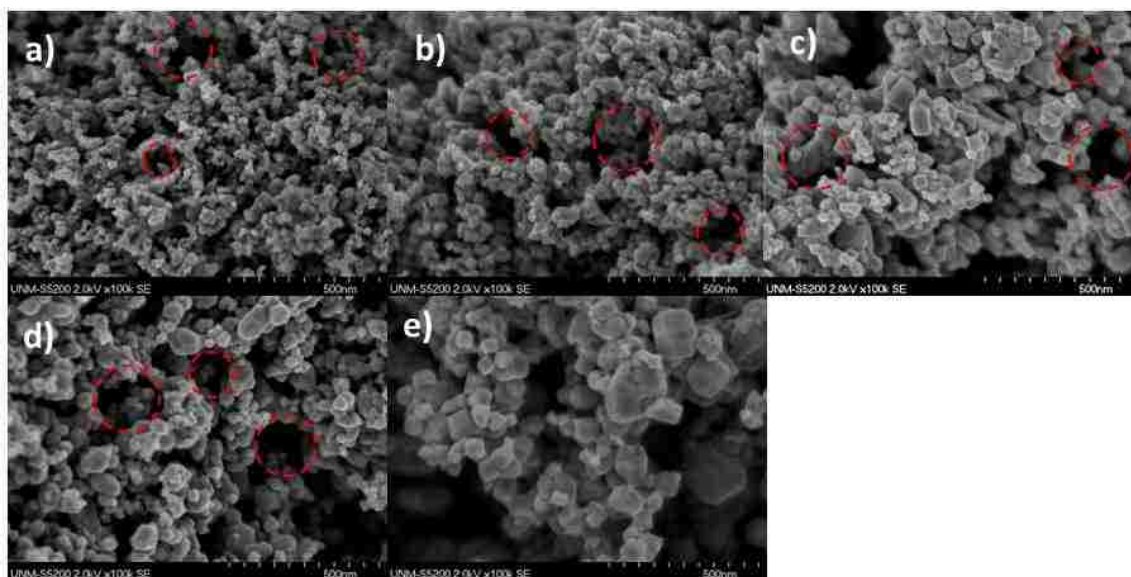


**Figure 7.** SEM images of the Cu nanoparticles synthesized at 250 °C in a 100% H<sub>2</sub> reduction: a) Cu<sub>B1</sub>, b) Cu<sub>B2</sub>, c) Cu<sub>B3</sub>, d) Cu<sub>B4</sub>, and e) Cu<sub>B5</sub>. The Cu<sub>B1</sub>, Cu<sub>B2</sub>, Cu<sub>B3</sub>, and Cu<sub>B4</sub> particles (a-d) exhibit sponge-like morphology consistent with the sacrificial support method (voids from EH-5 indicated in red).

7% and 100% H<sub>2</sub> reduction atmospheres smaller particles were synthesized for lower wt% of Cu in the precursor (Fig. 8). This may be due to dispersion of the Cu(NO<sub>3</sub>)<sub>2</sub> in a silica matrix, which deters the formation of larger particles with aggregation of smaller particles during the reduction step.

#### 4.1.2 Brunauer-Emmett-Teller surface area

The specific surface area for all catalysts, as measured by BET, are listed in Table 5. In general, the BET surface area decreases with increasing particle

size; this trend is particularly supported by the nearly identical surface areas of the Cu<sub>B3</sub> and Cu<sub>B4</sub> particles (11.4 vs. 11.8 m<sup>2</sup> g<sup>-1</sup>, respectively) and their similar average particle widths and distributions (48.6 ± 19.9 nm vs. 48.1 ± 20.9 nm, respectively).

**Table 6.** The mole percent (mol%) of Cu, CuO, and Cu<sub>2</sub>O, as determined from phase fitted XRD data for all particles synthesized using the sacrificial support method.

Sample (x)	Cu <sub>AX</sub>			Cu <sub>BX</sub>		
	Cu (mol %)	CuO (mol %)	Cu <sub>2</sub> O (mol %)	Cu (mol %)	CuO (mol %)	Cu <sub>2</sub> O (mol %)
1	25.2	12.7	62.2	32.5	0	67.5
2	47.0	1.58	51.4	51.9	8.47	39.7
3	15.7	-	84.3	46.4	12.1	41.5
4	67.6	-	32.4	20.8	-	79.2
5	76.2	4.61	19.2	52.9	-	47.1

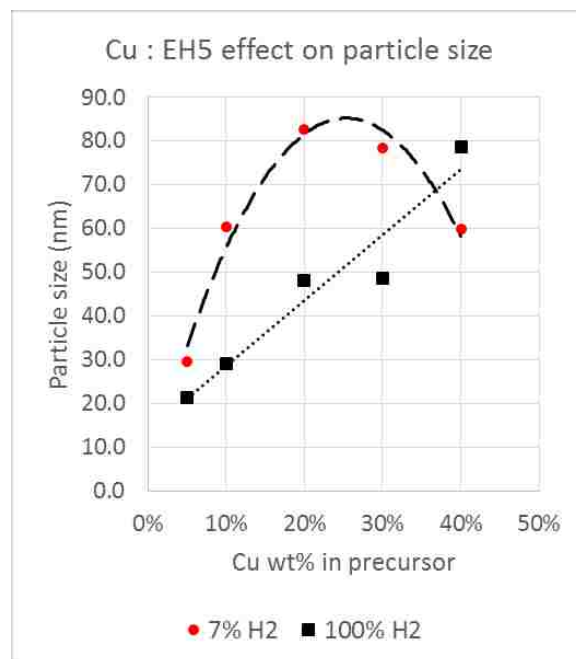


**Figure 8.** The effect of precursor Cu weight percent (wt%) on the average particle width during synthesis using the sacrificial support method.

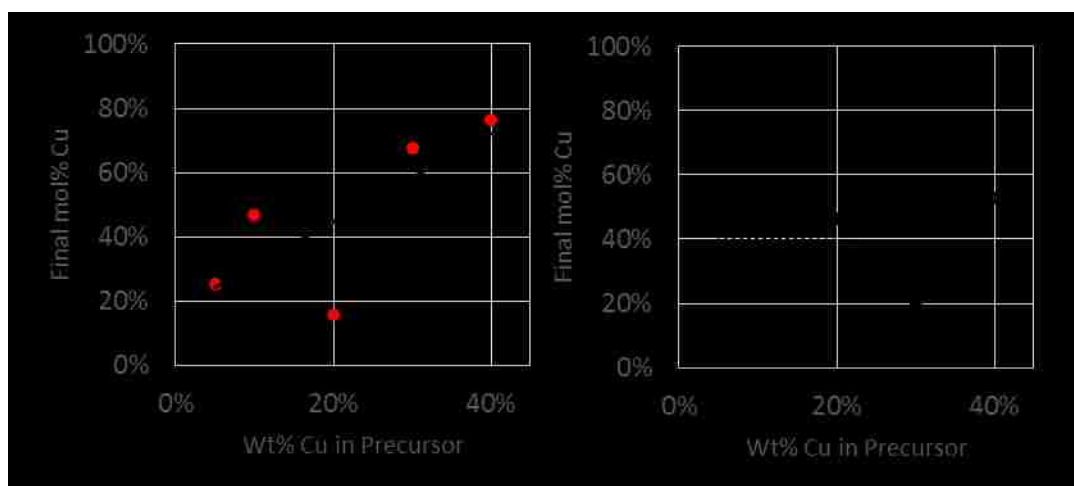


**Figure 9.** The effect of the precursor Cu weight percent and the reduction environment on the final  $\text{Cu}^0$  content in the particles prepared using the sacrificial support method where a) 100%  $\text{H}_2$  (250°C) and b) 7%  $\text{H}_2$  (350°C).

#### 4.1.3 X-ray diffraction

XRD patterns from all particles were fitted using Jade 2010 (MDI) to determine the mole percent (mol%) of Cu ( $\text{Cu}^0$ ),  $\text{Cu}_2\text{O}$  ( $\text{Cu}^+$ ), and CuO ( $\text{Cu}^{2+}$ ) in the materials (for XRD patterns see Appendix 2) and are listed in Table 6. From this point forward, Cu will be designated as  $\text{Cu}^0$  to distinguish it is not the same type of Cu as is present in the mono- or divalent Cu-oxides. No more than 13 mol% CuO was calculated for any particle, with the major phases  $\text{Cu}_2\text{O}$  and  $\text{Cu}^0$  exhibited in varied ratios. As previously discussed, the oxidation of  $\text{Cu}^0$  to CuO and  $\text{Cu}_2\text{O}$  is thermodynamically favorable in oxygen containing atmospheres at low temperatures and atmospheric pressure [59-62]. Additionally, although  $\text{Cu}^0$  forms from  $\text{Cu}(\text{NO}_3)_2$  after its decomposition there is a simultaneous formation of CuO and  $\text{Cu}_2\text{O}$  beginning at 200°C. Subsequent reduction of CuO to  $\text{Cu}_2\text{O}$ , and a final reduction of  $\text{Cu}_2\text{O}$  to  $\text{Cu}^0$  occurs between 200°C and 300°C [62]. Determining which of these two oxide formation sources accounts for the degree of

oxidation in these particles is difficult, but it is important to distinguish that a thin oxide layer formed in air and a particle consisting of significant quantities of oxides in its bulk will display different catalytic surfaces during electrochemical reduction. There appears to be no correlation between the wt% Cu in the precursor and the final mol% Cu<sup>0</sup> in the particles reduced in 100% H<sub>2</sub> (Fig. 9b). This suggests that the rate of oxide reduction is similar for all particles, at this temperature. The final mol% of Cu<sup>0</sup> for the particles reduced in 7% H<sub>2</sub> shows a positive correlation (Fig. 9a), with the highest Cu<sup>0</sup> content exhibited in the highest precursor wt% Cu (Cu<sub>A5</sub>, 76.2 mol% Cu<sup>0</sup>). The difference in trends can be attributed to the temperature of the reducing atmosphere. Until 250°C the effect of temperature would be identical for both atmospheres, because the temperature ramp rate for both reactions was the same (5°C min<sup>-1</sup>) – however, these particles were formed at different temperatures. While held at 250°C, the continued decomposition of gaseous intermediates would be accompanied by the slow reduction of oxides to Cu for the particles reduced in 100% H<sub>2</sub>. The eventual formation of Cu from its oxide forms does occur at this temperature, but may require a longer reduction period, even at such a high concentration of H<sub>2</sub>. The particles reduced in 7% H<sub>2</sub> were further heated to 350°C, undergoing the same reactions just discussed, but at a faster rate. The increase of final mol% Cu<sup>0</sup> for higher precursor Cu may be caused by rapid reduction of oxides (primarily Cu<sub>2</sub>O at this temperature) to Cu as the particle forms, because of the high temperature. So while more Cu<sup>0</sup> is formed at a higher temperature, during the same reduction time, the rate is accelerated to the point the particles begin to aggregate and overpower the template of silica, forming irregular sizes and shapes.

The particles with the highest Cu<sup>0</sup> mol% were formed at 350°C in low concentrations of H<sub>2</sub>, thus displaying the greatest extent of this precursor reduction, but they also are the largest and have the lowest BET surface area. The particles reduced in 100% H<sub>2</sub> at 250°C show a maximum Cu<sup>0</sup> content of c.a. 50 mol%, but in general less CuO. This suggests that a longer reduction time at the lower temperature and high H<sub>2</sub> concentration may increase the reduction of Cu<sub>2</sub>O to Cu<sup>0</sup> while maintaining the desired morphology.

## 4.2 Electrochemical characterization

### 4.2.1 Cyclic voltammetry

The electrochemical performance of the catalysts was tested in both diffusion and kinetically limited thin film regimes. Catalysts were initially screened by comparison of the cathodic sweep of cyclic voltammograms (CVs) captured at a scan rate of 20 mV s<sup>-1</sup> in N<sub>2</sub> and CO<sub>2</sub> saturated solutions (Appendix 3). For all catalysts the current density produced in a CO<sub>2</sub> saturated solution was less than in a N<sub>2</sub> saturated solution, an observation that confirms CER; a net decrease in current in the presence of CO<sub>2</sub> indicates competitive occupation of active sites of HER and CER.

Next, pseudo-steady state, diffusion limited performances were measured by cyclic voltammetry without rotation at a scan rate of 1 mV s<sup>-1</sup> (see Fig. 10-11). The maximum current densities of the Cu<sub>AX</sub> (X=1-5) particles range from -3.0 to -8.0 mA cm<sup>-2</sup> at -2.2 V vs. Ag/AgCl. The Cu<sub>A1</sub>, Cu<sub>A2</sub>, Cu<sub>A3</sub>, and Cu<sub>A5</sub> particles exhibit a characteristic limiting current at ca. -1.45 V vs. Ag/AgCl which has been previously identified as saturation of active sites by reduction of both H<sub>2</sub>O and CO<sub>2</sub> on Cu<sup>0</sup> surfaces (Fig. 10, inset) and can also be attributed to diffusion limitations of species to and from the

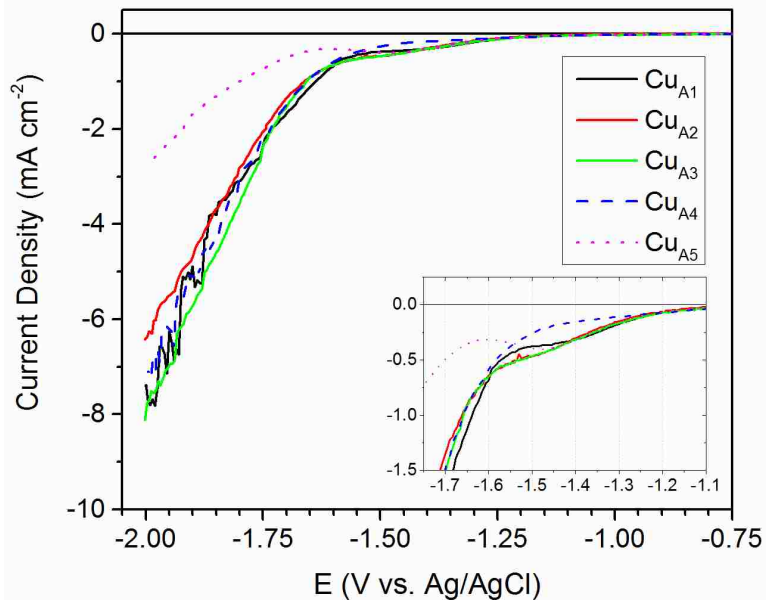


**Figure 10.** The cathodic sweep of voltammograms performed at  $1 \text{ mV s}^{-1}$  of Cu particles synthesized using SSM in 7%  $\text{H}_2$  at  $350^\circ\text{C}$  ( $\text{Cu}_{\text{Ax}}$ , where  $X=1-5$ ). Conditions:  $0.1\text{M KHCO}_3$ ,  $25^\circ\text{C}$ , no rotation.

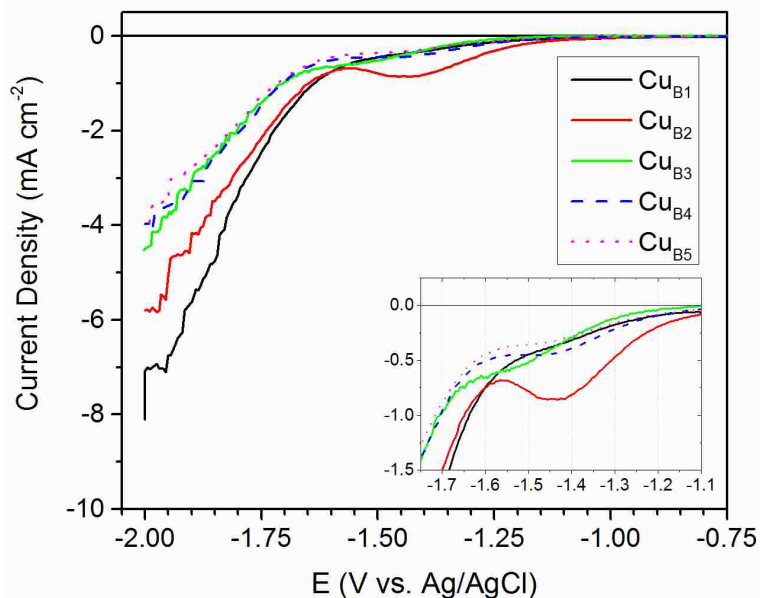


**Figure 11.** The cathodic sweep of voltammograms performed at  $1 \text{ mV s}^{-1}$  of Cu particles synthesized using SSM in 100%  $\text{H}_2$  at  $250^\circ\text{C}$ . ( $\text{Cu}_{\text{Bx}}$ , where  $X=1-5$ ). Conditions:  $0.1\text{M KHCO}_3$ ,  $25^\circ\text{C}$ , no rotation.

catalytic sites [41]. The Cu<sub>A5</sub> particles exhibit the highest inhibition of activity (a decrease of ca. 0.20 mA cm<sup>-2</sup>) from -1.45 to -1.65 V vs. Ag/AgCl (Fig. 10, inset), and have the lowest total current density (-2.5 mA cm<sup>-2</sup>). The high activity towards CER can be attributed to the high Cu<sup>0</sup> content in these particles (76.2 mol%), with the low performance due to the large particles size (60.0 ± 30.2), corresponding to a lower surface area and fewer catalytic sites. The current densities of Cu<sub>A1</sub>, Cu<sub>A2</sub>, Cu<sub>A3</sub>, and Cu<sub>A4</sub> particles are nearly identical from -1.75 to -2.00 V vs. Ag/AgCl. Differences are visible in the slope of their limiting currents (Fig. 10, inset). The Cu<sub>A1</sub> particles exhibit a constant limiting current density for ca. 35 mV until it begins to increase at -1.55 V vs. Ag/AgCl. The Cu<sub>A2</sub> and Cu<sub>A3</sub> particles exhibit a constant slope in current densities from -1.30 to -1.60 V vs. Ag/AgCl before it begins to increase, with a slight inflection at -1.45 V vs. Ag/AgCl indicating a limiting current density. The Cu<sub>A4</sub> particles do not show any inflection to indicate the competitive activity of CER, instead slowly increasing in current density until -1.55 V vs. Ag/AgCl. These particles are dissimilar in size, composition and morphology, so it is likely the similarity in current is due to diffusion limitations – which is more visible for the smaller particles (Fig. 6a) than for larger particles with a more open framework (Fig. 6b-6d). This diffusion limitation depends on the activity of the catalyst, as is evident from differences observed near the onset of CER (ca. -1.20 V vs. Ag/AgCl), but to what extent the activity of these particles varies is unclear from this data.

The maximum current densities of the Cu<sub>BX</sub> (X=1-5) particles range from -4 to -8.0 mA cm<sup>-2</sup> at -2.0 V vs. Ag/AgCl (Fig. 11). The Cu<sub>B2</sub>, Cu<sub>B4</sub>, and Cu<sub>B5</sub> particles exhibit the

characteristic limiting current near  $-1.45$  V vs. Ag/AgCl, while the  $\text{Cu}_{\text{B}3}$  particles exhibit a limiting current at ca.  $-1.55$  V vs. Ag/AgCl (Fig. 11, inset). The  $\text{Cu}_{\text{B}1}$  particles exhibit the highest current density ( $-8.0$  mA  $\text{cm}^{-2}$ ) with a downward inflection between  $-1.30$  and  $-1.55$  V vs. Ag/AgCl, before exhibiting a sharp increase in current density. This inflection could correspond to a low amount of CER activity, but is not conclusive. The  $\text{Cu}_{\text{B}2}$  particles exhibit the second highest current density, with a distinct limiting current at  $-1.45$  V vs. Ag/AgCl, previously attributed to high  $\text{Cu}^0$  content (in the  $\text{Cu}_{\text{A}5}$  particles, Fig. 10 inset), which agrees well with the relatively high  $\text{Cu}^0$  content in these particles (51.9 mol%). The current densities of the  $\text{Cu}_{\text{B}3}$ ,  $\text{Cu}_{\text{B}4}$ , and  $\text{Cu}_{\text{B}5}$  particles are nearly identical after  $-1.75$  V vs. Ag/AgCl, with a maximum of ca.  $-4.0$  mA  $\text{cm}^{-2}$ ; prior to this potential, differences in activity are visible starting at  $-1.20$  V vs. Ag/AgCl (Fig. 11, inset). The  $\text{Cu}_{\text{B}3}$  particles exhibit the lowest current until  $-1.40$  V vs. Ag/AgCl after which its current density is higher than both  $\text{Cu}_{\text{B}4}$  and  $\text{Cu}_{\text{B}5}$  ( $0.25$  mA  $\text{cm}^{-2}$ ), reaching an inflection point and a slowing rate of increasing current density at ca.  $-1.55$  V vs. Ag/AgCl. The  $\text{Cu}_{\text{B}4}$  and  $\text{Cu}_{\text{B}5}$  particles exhibit similar behavior between  $-1.30$  and  $-1.60$  V vs. Ag/AgCl. However, the limiting current density of the  $\text{Cu}_{\text{B}4}$  particles is more pronounced (ca.  $-0.5$  mA  $\text{cm}^{-2}$ ) than that of the  $\text{Cu}_{\text{B}5}$  particles – this behavior is unexpected considering their relative  $\text{Cu}^0$  content (20.8 mol%, 52.9 mol% respectively) which would suggest a reverse relationship. This reveals a significant shortcoming when relying on XRD compositional analysis of these particles – its bulk analysis does little to describe the surface species and suggests further surface sensitive analysis would be beneficial to understanding the surface concentrations of  $\text{Cu}^0$ ,  $\text{Cu}^+$ , and  $\text{Cu}^{2+}$ , especially in cases where the previously



observed behavior of the electrochemical performance of  $\text{Cu}^0$  is contradicted. The consistent morphology of the particles reduced in 100%  $\text{H}_2$  illuminates some effect due to particle size, with a clear increase in current densities for smaller particles, but the degree to which this is influenced by concurrent restrictions to catalytic sites developed under diffusion limitations is unclear from this data.

#### 4.2.2 Bulk electrolysis

The electrochemical stability of the catalysts was tested by bulk electrolysis at three potentials of interest: -1.2, -1.6 and -2.2 V vs. Ag/AgCl. At -1.2 V vs. Ag/AgCl, the relative onset of CER can be determined; this is very near the theoretically calculated rate limiting potential of 0.74 V vs. SHE, associated with the reduction of a  $\text{CO}_{\text{ad}}$  to a carbonyl proposed by Peterson and Norskov [39]. It is expected that the major product at this potential will be  $\text{H}_2$ . Many fundamental studies report CER at -1.6 V vs. Ag/AgCl, with current densities of 3-5  $\text{mA cm}^{-2}$  on polycrystalline Cu and can thus serve as a benchmark for comparison (Table 1) [25, 42, 47-48]. Substantial quantities of CER gas phase products have been reported in studies at -2.2 V vs. Ag/AgCl, and thus can illuminate more realistic limits of conversion for appreciable quantities of CER and the energetic cost of associated current densities. Stability at all potentials is important, as it indicates the surface is chemically stable in the entire CER potential range, but is especially important at -1.6 and -2.2 V vs. Ag/AgCl because these are the potentials which are associated with measurable quantities of CER products that are essential to determine selectivity towards observed products by quantification of gas, liquid, or both gas and liquid phases as previously discussed. To this end, bulk electrolysis was

performed for 1 hour with and without rotation. The experiments without rotation were performed to determine if diffusion limited pseudo-steady state CVs are predictive of actual steady state performance. Experiments with rotation were performed to determine the kinetically limited steady state current, and to confirm stability to allow for quantification of gas products.

The current densities of all particles reached and maintained a steady current density for the duration of the diffusion limited experiments (Appendix 4). Comparison of the steady state and pseudo-steady state performance of the particles for both 7% and 100% H<sub>2</sub> reduction atmospheres indicates that the steady state current densities predicted at -1.2 and -1.6 V vs. Ag/AgCl by slow scan voltammetry at 1 mV s<sup>-1</sup> are not indicative of either rank of performance or actual current densities under potentiostatic conditions (Fig. 12). Bulk electrolysis current densities are reported as 30 minute averages, while voltammogram current densities are reported as averages of ± 20 mV of the potential state.

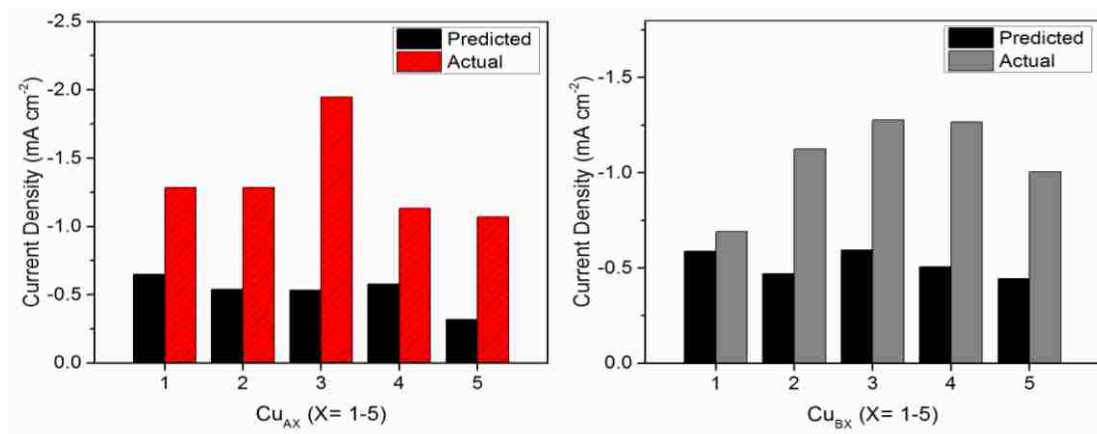


**Figure 12.** Comparison of average current densities from particles reduced in a) Cu<sub>Ax</sub> and b) Cu<sub>Bx</sub> (X=1-5) for bulk electrolysis and slow scan voltammetry at -1.6 V vs. Ag/AgCl illustrating the discrepancies between expected and observed steady state values.

The steady state performance of the  $\text{Cu}_{\text{AX}}$  and  $\text{Cu}_{\text{BX}}$  ( $X=1-5$ ) particles were tested to observe their kinetically limited current densities at  $-1.6$  and  $-2.2$  V vs. Ag/AgCl (Fig. 13-14) while held for 1 hour. Current densities under rotation were greater than those without, as is expected for a system with diffusion limitations. The magnitude of the current densities (10s of  $\text{mA cm}^{-2}$ ) produced are comparable to those reported by Baturina et al. for similar catalyst loadings ( $20 \mu\text{g cm}^{-2}$ ) [42].

The  $\text{Cu}_{\text{AX}}$  ( $X=1-5$ ) particles were relatively stable when held for one hour at  $-1.6$  V vs. Ag/AgCl (Fig. 13a) and very stable when held for one hour at  $-2.2$  V vs. Ag/AgCl (Fig. 13b). While held at  $-1.6$  V vs. Ag/AgCl the  $\text{Cu}_{\text{A1}}$  and  $\text{Cu}_{\text{A2}}$  particles exhibited a stable current density after 20 minutes, the  $\text{Cu}_{\text{A4}}$  particles exhibited a continuously increasing current density (although the rate of increase slowed after 30 minutes), and the  $\text{Cu}_{\text{A3}}$  and  $\text{Cu}_{\text{A5}}$  particles exhibit a very stable current density after several minutes. The improvement of current in the  $\text{Cu}_{\text{A1}}$ ,  $\text{Cu}_{\text{A2}}$ , and  $\text{Cu}_{\text{A4}}$  particles is

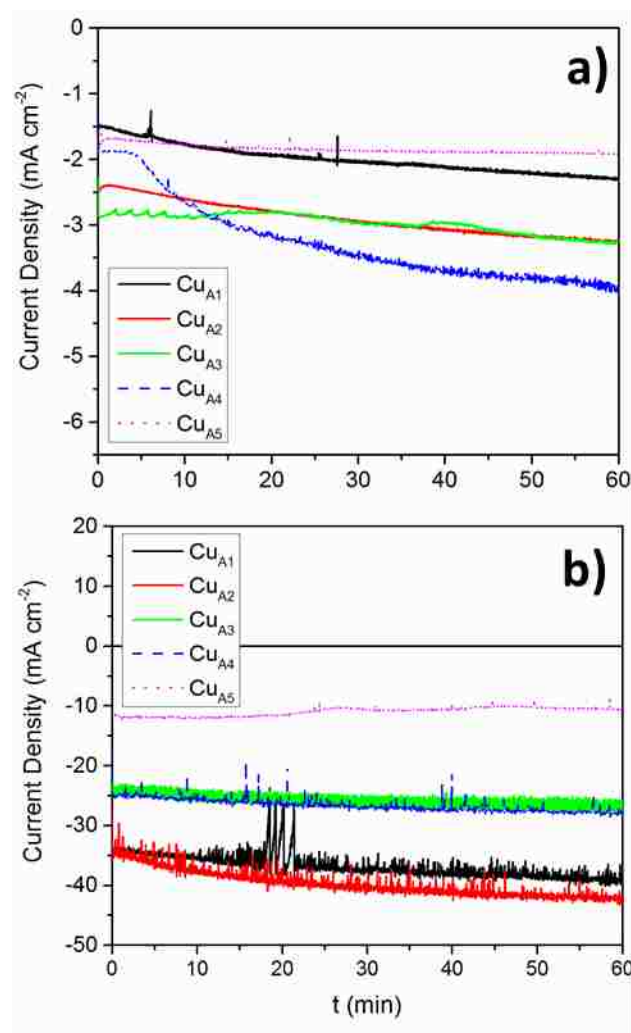


**Figure 13.** Bulk electrolysis of Cu particles reduced at  $350^\circ\text{C}$  in a 7%  $\text{H}_2$  atmosphere at a)  $-1.6$  and at b)  $-2.2$  V vs. Ag/AgCl. Conditions:  $0.1\text{M KHCO}_3$ , 1600 RPM,  $25^\circ\text{C}$ .

likely due to reduction of reordering of the catalyst surface at this negative potential. Recall that surface oxides begin to be electrochemically reduced after -0.60 V vs. Ag/AgCl, as discussed by Peterson [38], thus all surface oxides should be completely reduced to Cu<sup>0</sup>, but the facets exposed may be unstable since they are essentially patterned from oxygen vacancies [46-47]. This process increases the current densities of the Cu<sub>A1</sub> and Cu<sub>A2</sub> particles less (an increase of ca. 0.50 mA cm<sup>-2</sup>) than for the Cu<sub>A4</sub> particles (an increase of ca. 2.0 mA cm<sup>-2</sup>). It unclear why the Cu<sub>A4</sub> particles experience such a dramatic improvement in current density, since they possess a high Cu<sup>0</sup> content (67.2 mol%), and would thus be expected to have a more stable surface (as in the Cu<sub>A5</sub> particles, which are 76.2 mol% Cu<sup>0</sup>). The stability of the Cu<sub>A3</sub> and Cu<sub>A5</sub> particles may be due to both possessing ca. 80 mol% of a single phase (Cu<sub>2</sub>O and Cu, respectively), which may lend increased resistance of these particles against substantial surface reordering after a brief reduction of a thin oxide layer. While held at -2.2 V vs. Ag/AgCl, the Cu<sub>A1</sub> and Cu<sub>A2</sub> particles achieve stable current densities after 20 minutes, exhibiting similar behavior as observed at -1.6 V vs. Ag/AgCl. The Cu<sub>A3</sub>, Cu<sub>A4</sub>, and Cu<sub>A5</sub> particles are immediately stable, remaining at near constant current densities for the duration of the experiment. The rapidity of this stabilization can be attributed to the very high potential of this electrolysis, any surface changes occurring would be expected to occur more quickly at lower potentials. The changes in current density performance ranks at -1.6 and -2.2 V vs. Ag/AgCl are noticeably different, and allude to differences in reduction mechanism, but further deductions from this observation are not possible with this data.

The  $\text{Cu}_{\text{B}X}$  ( $X=1-5$ ) particles were relatively stable when held for one hour at  $-1.6$  V vs. Ag/AgCl (Fig. 14a) and very stable when held at  $-2.2$  V vs. Ag/AgCl (Fig. 14b). The  $\text{Cu}_{\text{B}1}$ ,  $\text{Cu}_{\text{B}2}$ , and  $\text{Cu}_{\text{B}3}$  particles exhibit increasing current densities; the  $\text{Cu}_{\text{B}1}$  particles stabilize at 15 minutes, while the  $\text{Cu}_{\text{B}2}$  and  $\text{Cu}_{\text{B}3}$  particles both asymptotically approach a maximum value by the lapse of an hour. For these particles, the final current density is more than doubled the initial current density.

As discussed previously (for the  $\text{Cu}_{\text{A}1}$  and  $\text{Cu}_{\text{A}2}$  particles, Fig. 12a)

this is likely due to electrochemical reordering of the catalyst surface. The  $\text{Cu}_{\text{B}4}$  and  $\text{Cu}_{\text{B}5}$  particles stabilize in minutes and remain so for the duration of the experiment. Again, there is no apparent correlation between the  $\text{Cu}^0$  and  $\text{Cu}_2\text{O}$  content and the relative stability of these particles. When held at  $-2.2$  V vs. Ag/AgCl for 1 hour, all particles were stable after 20 minutes. As observed for the  $\text{Cu}_{\text{A}X}$  ( $X=1-5$ ) particles, performance ranks of

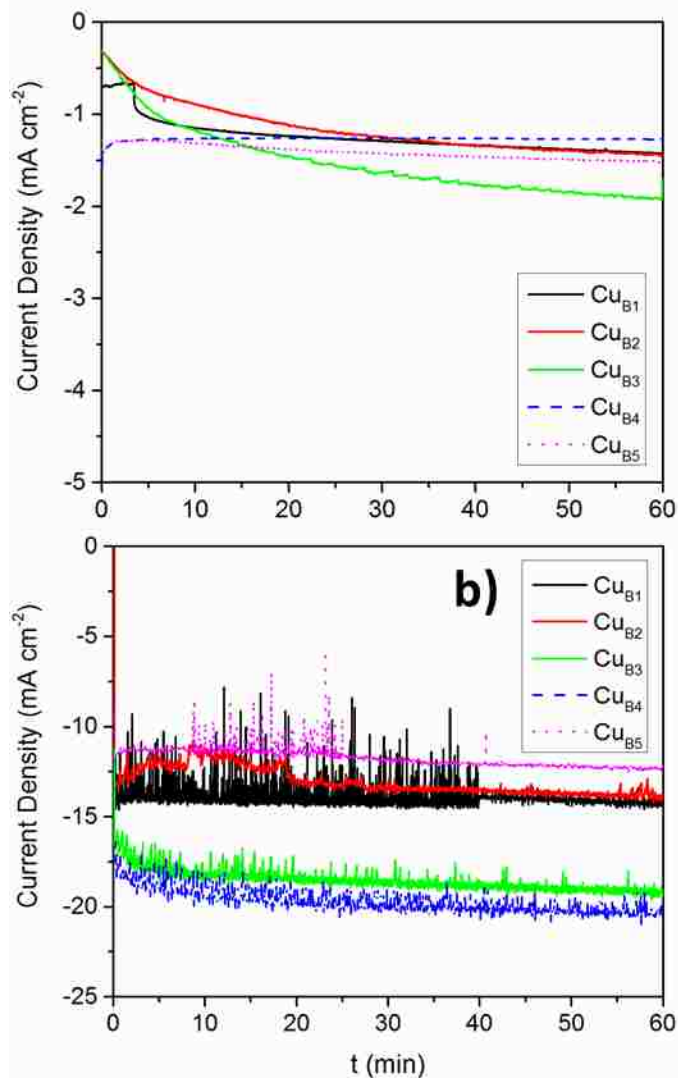


**Figure 14.** Bulk electrolysis of Cu particles reduced at  $250^\circ\text{C}$  in a  $100\%$   $\text{H}_2$  atmosphere at a)  $-1.6$  and at b)  $-2.2$  V vs. Ag/AgCl. Conditions:  $0.1\text{M}$   $\text{KHCO}_3$ ,  $1600$  RPM,  $25^\circ\text{C}$ .

these particles are inconsistent between -1.6 and -2.2 V vs. Ag/AgCl, consistent with different CER reduction pathways at different potentials.

#### 4.3 Correlations between electrochemical performance material properties

To understand how performances relate to material properties, possible correlations between  $\text{Cu}^0$  content and BET surface area were explored (Fig. 15-18). (Note: BET surface areas were previously correlated with particle size, where higher surface areas are associated with smaller particle size listed on Table 5, and as such particle size will not be explicitly compared because it is redundant.) The  $\text{Cu}_{\text{AX}}$  (X=1-5) particles exhibit decreasing current density at both -1.2 (Fig. 15, top) and -2.2 V vs. Ag/AgCl (Fig. 15, bottom) as  $\text{Cu}^0$  content increases, with no clear effect for -1.6 V vs. Ag/AgCl (Fig. 15, middle). Recall that -1.2 V vs. Ag/AgCl is the potential at which CER begins, but  $\text{H}_2$  production dominates because of energy barriers to reduction of adsorbed CER intermediates [38-39]. A decrease in current can correspond to reduction of HER by this mechanism. At decrease in current at -2.2 V vs. Ag/AgCl can be attributed to competitive reduction by CER and HER, hence a decrease in the slope of this correlation. The magnitude of the current densities generated by all particles at -1.6 V vs. Ag/AgCl are comparable to those reported for polycrystalline Cu (-2.0 to -4.0 mA  $\text{cm}^{-2}$ , Table 1). At this potential the energy barrier to reduction of  $\text{CO}_{\text{ad}}$  is overcome, and multiple pathways open – this may account for the inconclusive current densities observed; while CER is likely occurring at a more rapid rate, the adsorption affinities of intermediates and products may obscure this effect. A reverse trend is observed for BET surface area, with increasing current density corresponding to higher surface area for

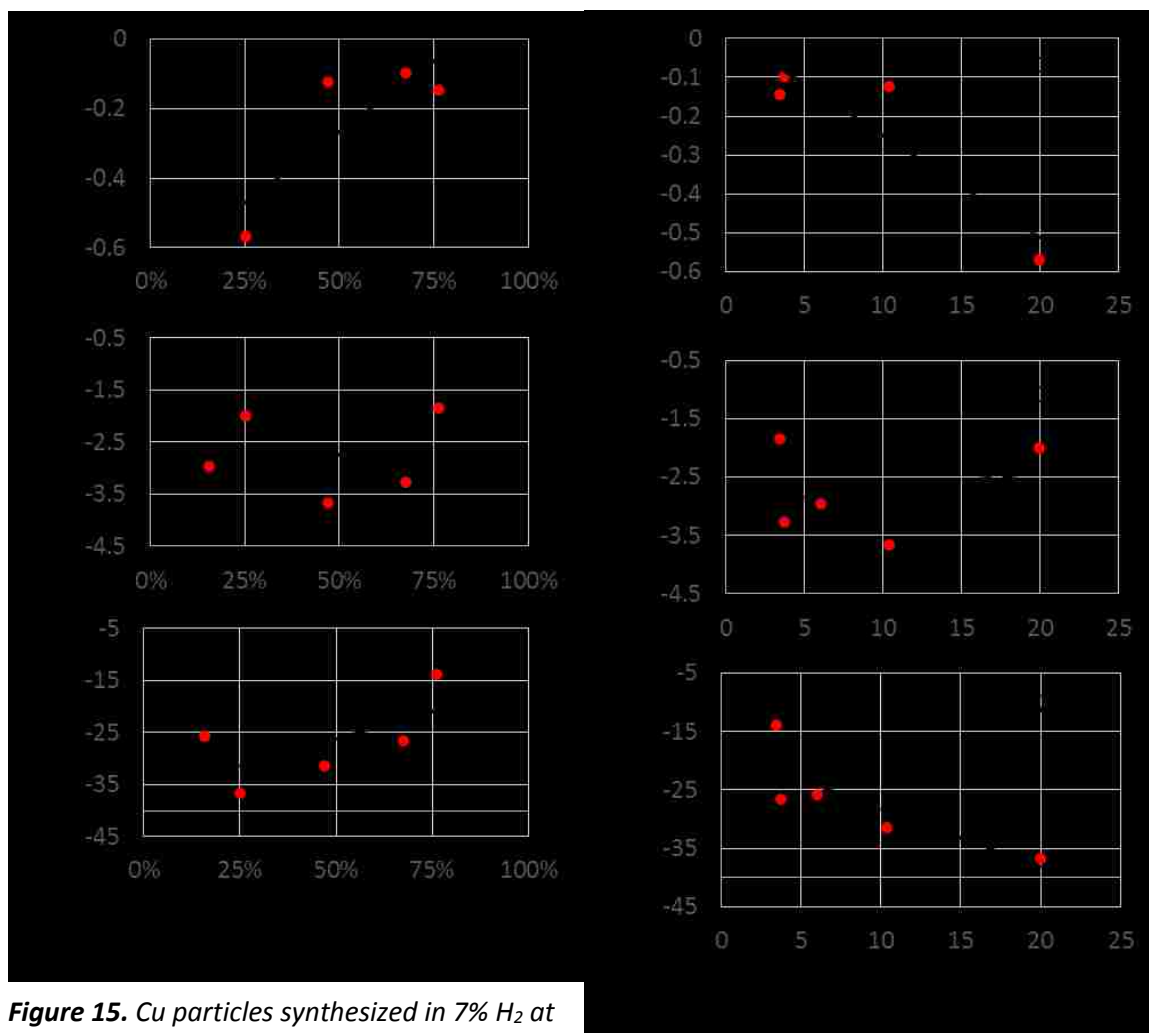


**Figure 15.** Cu particles synthesized in 7% H<sub>2</sub> at 350°C exhibit decreasing current density as Cu<sup>0</sup> content increases at -1.2 (top) and -2.2 (bottom), with no apparent correlation at -1.6 (middle) V vs. Ag/AgCl. Conditions: 0.1M KHCO<sub>3</sub>, 1600 RPM, 25°C.

**Figure 16.** Cu particles synthesized in 7% H<sub>2</sub> at 350°C exhibit increasing current density for increasing BET surface area at -1.2 (top) and -2.2 V vs. Ag/AgCl (bottom), with no clear effect at -1.6 (middle) V vs. Ag/AgCl. Conditions: 0.1M KHCO<sub>3</sub>, 1600 RPM, 25°C.

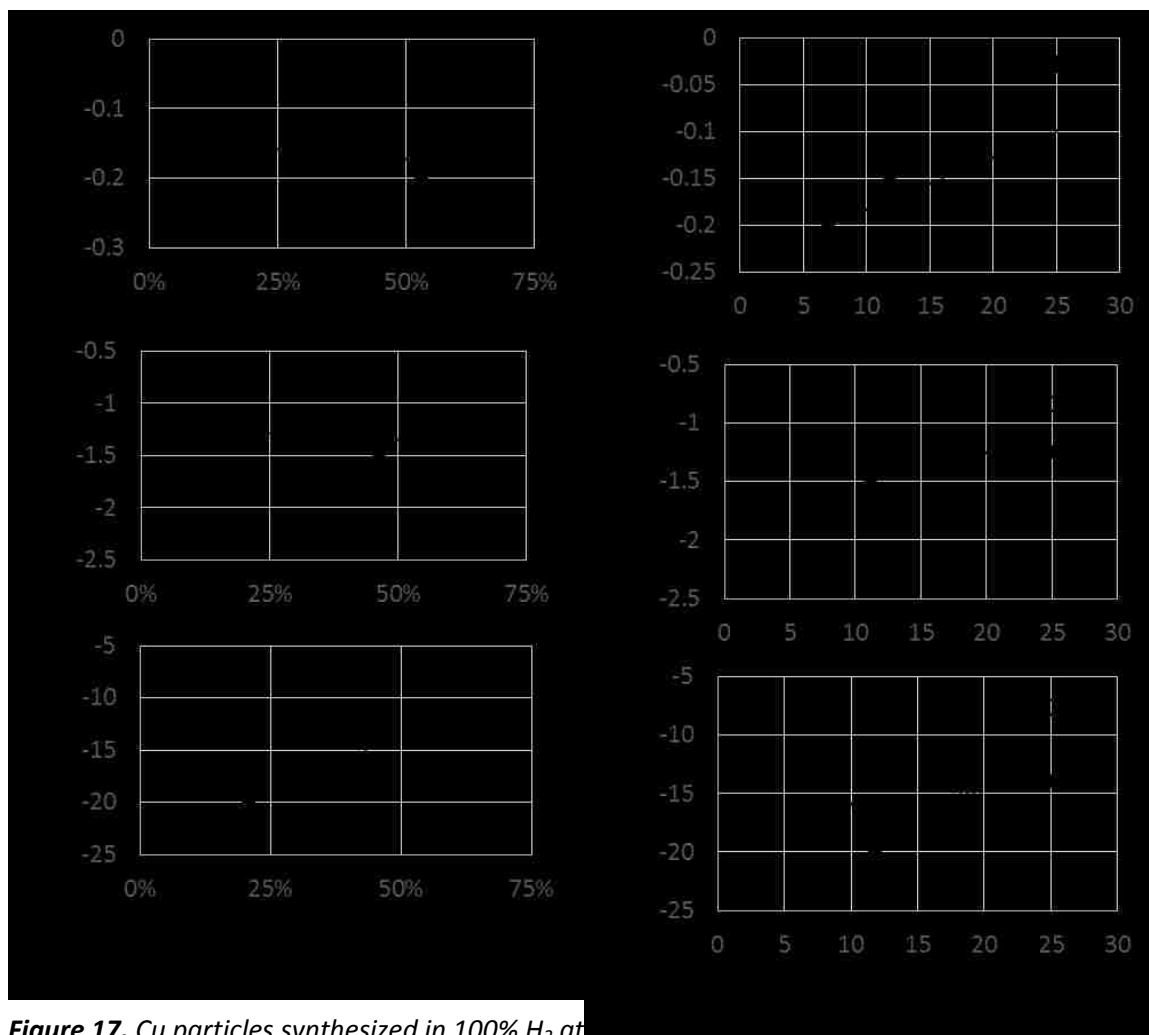


**Figure 17.** Cu particles synthesized in 100% H<sub>2</sub> at 250°C exhibit decreasing current for increasing Cu<sup>0</sup> content at -2.2 (bottom), with no apparent correlation at -1.2 (top) and -1.6 (middle) V vs. Ag/AgCl. Conditions: 0.1M KHCO<sub>3</sub>, 1600 RPM, 25°C.

**Figure 18.** Cu particles synthesized in 100% H<sub>2</sub> at 250°C exhibit decreasing current density for increasing BET surface area at -1.2 (top) and -1.6 (middle), with near clear effect at -2.2 (bottom) V vs. Ag/AgCl. Conditions: 0.1M KHCO<sub>3</sub>, 1600 RPM, 25 °C.



-1.2 and -2.2 V vs. Ag/AgCl (Fig. 16, top and bottom); these observations are consistent with behaviors observed in CVs – higher Cu<sup>0</sup> results in competitive CER/HER, thus reducing net current but also corresponds to larger particles (and correspondingly lower surface areas), while smaller particles increase surface area and access to catalytic sites resulting in increased total current. From these observations, the highest performing catalyst should have both high Cu<sup>0</sup> content and high surface area to maximize CER, which corresponds to the Cu<sub>A2</sub> particles, which were thus selected for further testing by gas chromatography.

The Cu<sub>BX</sub> (X=1-5) particles exhibit increasing current for increasing Cu<sup>0</sup> content at -2.2 V vs. Ag/AgCl, with no clear trend for -1.2 and -1.6 V vs. Ag/AgCl (Fig. 17). At -1.2 V vs. Ag/AgCl there is no obvious suppression of HER as in the previous case (Fig. 15), which may be attributed to the similar surface chemistries of these particles near the onset of CER (i.e., they are producing H<sub>2</sub> at similar rates, and may be inhibited at similar rates as well) but this cannot be conclusively asserted. The magnitude of the current densities generated by all particles at -1.6 V vs. Ag/AgCl is between -1.0 and -1.5 mA cm<sup>-2</sup>, slightly lower than those typically reported for polycrystalline Cu (lowest: 2.5 mA cm<sup>-2</sup>, Table 1). As with the Cu<sub>AX</sub> (X=1-5) particles, this can signify a complex interplay between adsorbed intermediates, products, and HER, but cannot signify any one specific cause. Although less persuasive than the previous case, this could suggest CER suppression of HER, as previously discussed, at -2.2 V vs. Ag/AgCl. Current densities decrease slightly for higher BET surface areas at -1.2 V vs. Ag/AgCl, with no clear trend observed at -1.6 and -2.2 V vs. Ag/AgCl (Fig. 18). This could indicate competitive

CER/HER rates on higher surface areas, but is not conclusive. A lack of clear trends in this material set necessitates implementing the same criteria applied to the previous particles: the particles with the highest  $\text{Cu}^0$  content and the highest surface area were  $\text{Cu}_{\text{B}2}$ , and thus were selected for further testing of gas phase products.

## 5. Conclusions

The synthesis of Cu nanoparticles using the SSM method is promising. Implementation of this synthesis method to develop particles with a controlled and specifically structured morphology was successfully achieved for lower precursor Cu contents (5wt% and 10wt%) in both reduction environments. The Cu<sub>A1</sub> and Cu<sub>A2</sub> were within the typical Cu nanoparticle range (15-100 nm) with widths of  $29.8 \pm 9.4$  and  $69.5 \pm 21.5$  nm, respectively, although their Cu<sup>0</sup> content was correspondingly low – 25.2 and 47.0 mol%, respectively. Comparatively, the Cu<sub>B1</sub> and Cu<sub>B2</sub> particles exhibited an even higher degree of control over morphology with smaller particle widths,  $21.5 \pm 9.4$  nm and  $29.3 \pm 21.5$  nm, respectively. However, these particles were similarly low in final molar Cu<sup>0</sup> content, with 32.5 and 51.9 mol%, respectively. The consistently high amount of oxidation for these particles may be mediated by modifications to the synthesis approach such as completely evaporating water vapor from precursors prior to synthesis at low temperatures, exploring more complex temperature treatments (involving multiple temperature and time intervals), and developing a more controlled method of passivation after reduction, which may all optimize the final Cu<sup>0</sup> content while maintaining the desired morphology. Further, studies into the surface content of these particles may reveal if such concerns are even necessary, since Cu<sub>2</sub>O has been shown to be catalytically active towards CER [42,46-47]. When tested for electrochemical stability, the Cu<sub>A1</sub>, Cu<sub>A2</sub>, Cu<sub>B1</sub>, and Cu<sub>B2</sub> particles were adequately stable when bulk electrolysis was performed for 1 hour at -1.6 and -2.2 V vs. Ag/AgCl (Fig. 13-14). This confirms they are suitable for further analysis of gas and liquid phase products

to determine their selectivity towards specific CER products. These particles exhibit higher current densities when a kinetically limited regime, as is typical of a system with diffusion limitations, although this is not necessarily a negative attribute since it may increase the residence time of intermediates and increase product selectivity towards a single product. This can be determined by further studies that quantify liquid and gas phase products of the  $\text{Cu}_{\text{A}2}$  and  $\text{Cu}_{\text{B}2}$  nanoparticles. The highest current densities at -2.2 V vs. Ag/AgCl were ca.  $-40 \text{ mA cm}^{-2}$  for  $\text{Cu}_{\text{A}2}$  and ca.  $-35 \text{ mA cm}^{-2}$  for  $\text{Cu}_{\text{A}1}$ . The  $\text{Cu}_{\text{B}1}$  and  $\text{Cu}_{\text{B}1}$  particles exhibited lower current densities of ca.  $-15 \text{ mA cm}^{-2}$ . These are all of the same magnitude of current densities reported for similar catalyst loadings and in similar conditions for carbon supported Cu [42] but are significantly more stable, suggesting this synthesis method may achieve even higher current densities once optimized for higher  $\text{Cu}^0$  content and can be deployed in a bench-scale fuel cell apparatus.

## APPENDICES

**Appendix 1.** Particle size, defined as the length of the chord for non-spherical particles and diameter for spherical particles, distributions of Cu nanoparticles synthesized using the SSM, as determined by SEM.

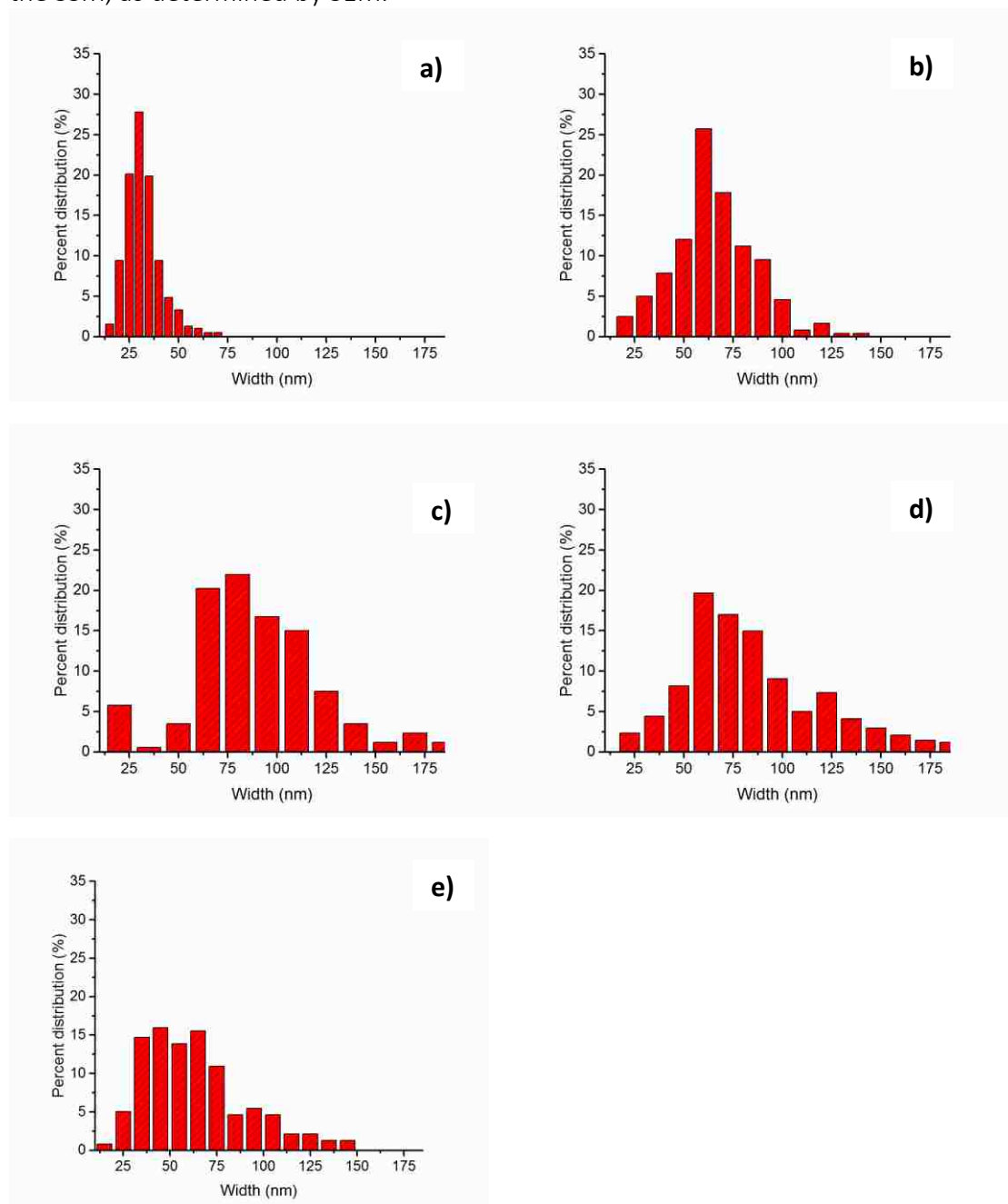


**Figure 19.** Particle width distributions of Cu synthesized in 7%  $H_2$  at 250°C: a)  $Cu_{A1}$ , b)  $Cu_{A2}$ , c)  $Cu_{A3}$ , d)  $Cu_{A4}$ , e)  $Cu_{A5}$ . The  $Cu_{A1}$ ,  $Cu_{A2}$ , and  $Cu_{A3}$  particles appear to have a normal distribution (a-c);  $Cu_{A4}$  (d) is skewed left and exhibits two populations at ca. 60 and 118, while  $Cu_{A5}$  (e) similarly exhibits a skewed left distribution with two populations at ca. 55 nm and 95 nm.

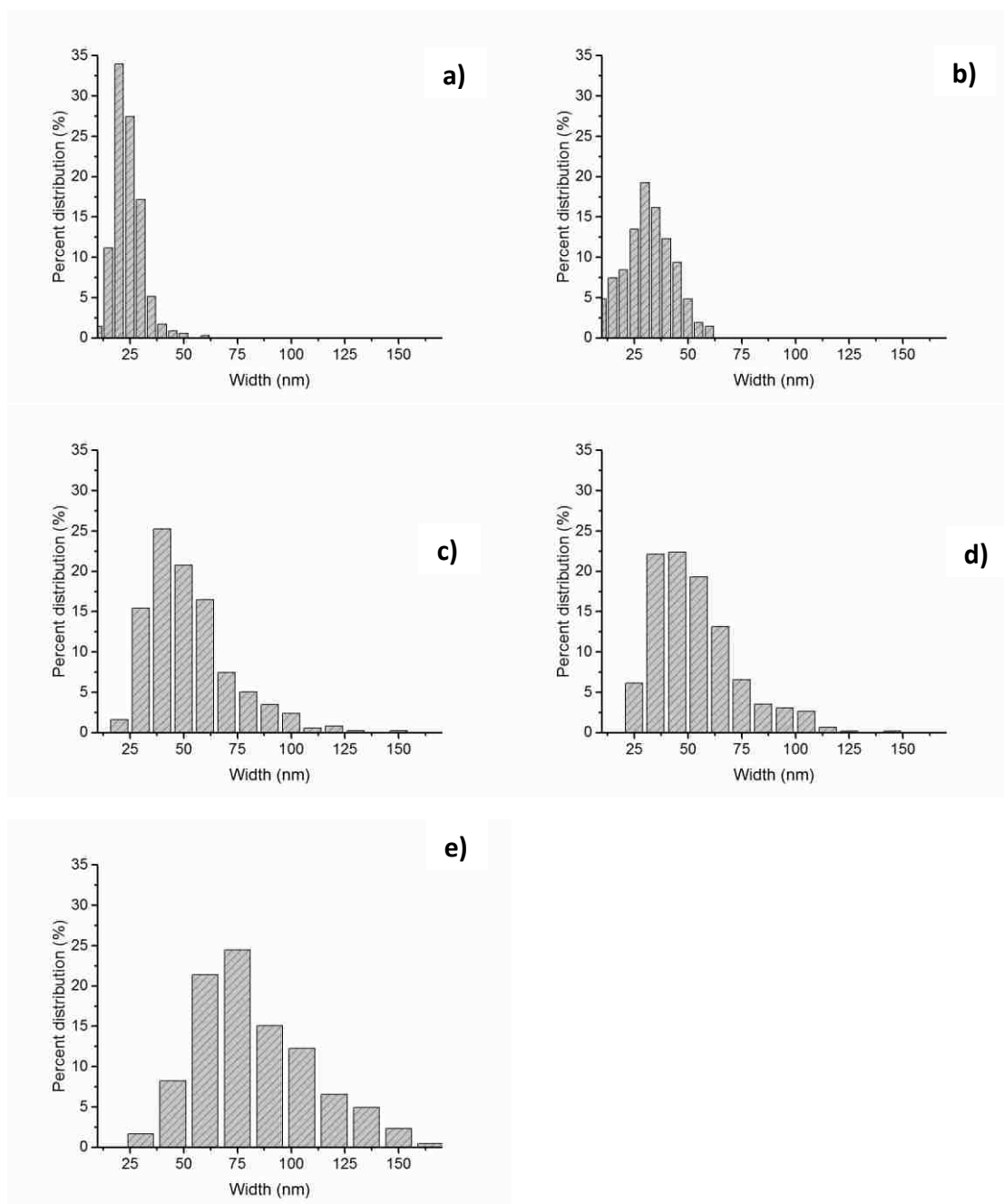


**Figure 20.** Particle width distributions of Cu synthesized in 100% H<sub>2</sub> at 350 °C: a) Cu<sub>B1</sub>, b) Cu<sub>B2</sub>, c) Cu<sub>B3</sub>, d) Cu<sub>B4</sub>, e) Cu<sub>B5</sub>. The Cu<sub>B1</sub> and Cu<sub>B2</sub> (a-b) particles appear to have a normal distribution. The Cu<sub>B3</sub>, Cu<sub>B4</sub>, and Cu<sub>B5</sub> (c-e) distributions are skewed left, but exhibit singular population means (ca. 40, 45, and 75 nm respectively).

**Appendix 2.** XRD patterns taken of Cu nanoparticles synthesized using the SSM.

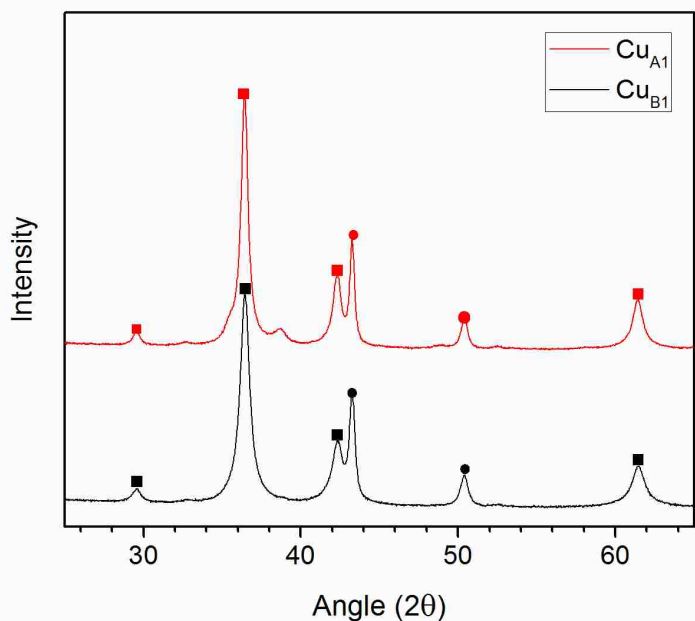


**Figure 21.** XRD patterns of catalysts prepared from 5wt% Cu precursors in 7% ( $\text{Cu}_{A1}$ , red) and 100%  $\text{H}_2$  ( $\text{Cu}_{B1}$ , black) atmospheres.  $\text{Cu}_2\text{O}$  (squares):  $29.6^\circ - (110)$ ,  $36.4^\circ - (111)$ ,  $42.3^\circ - (200)$ ,  $61.4^\circ - (220)$ . Cu (circles):  $43.2^\circ - (111)$ ,  $50.4^\circ - (200)$ . CuO is a minor phase included in refinements for the particles reduced in 7%  $\text{H}_2$ , at 12.7mol%.

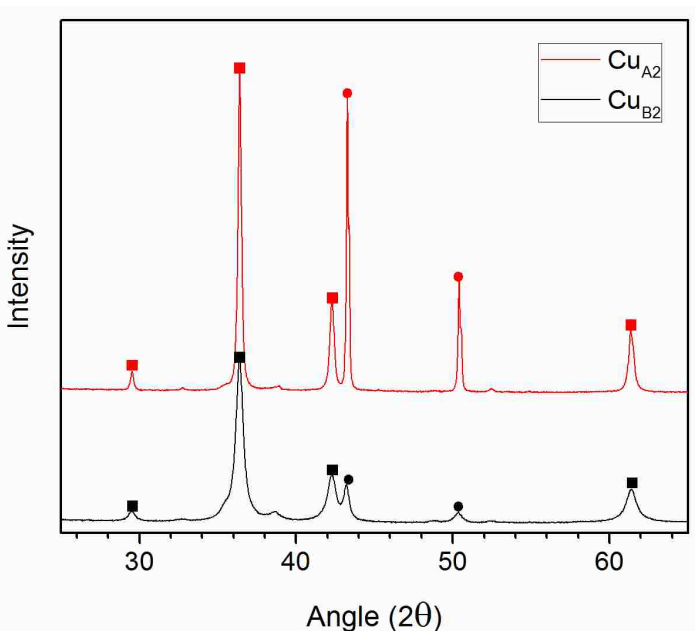


**Figure 22.** XRD patterns of catalysts prepared from 10wt% Cu precursors in 7% ( $\text{Cu}_{A2}$ , red) and 100%  $\text{H}_2$  ( $\text{Cu}_{B2}$ , black) atmospheres.  $\text{Cu}_2\text{O}$  (squares):  $29.6^\circ - (110)$ ,  $36.4^\circ - (111)$ ,  $42.3^\circ - (200)$ ,  $61.4^\circ - (220)$ . Cu (circles):  $43.2^\circ - (111)$ ,  $50.4^\circ - (200)$ . CuO is a minor phase included in refinements for the particles reduced in 7%  $\text{H}_2$  and 100%  $\text{H}_2$ , at 1.58 at 8.47 mol%, respectively.

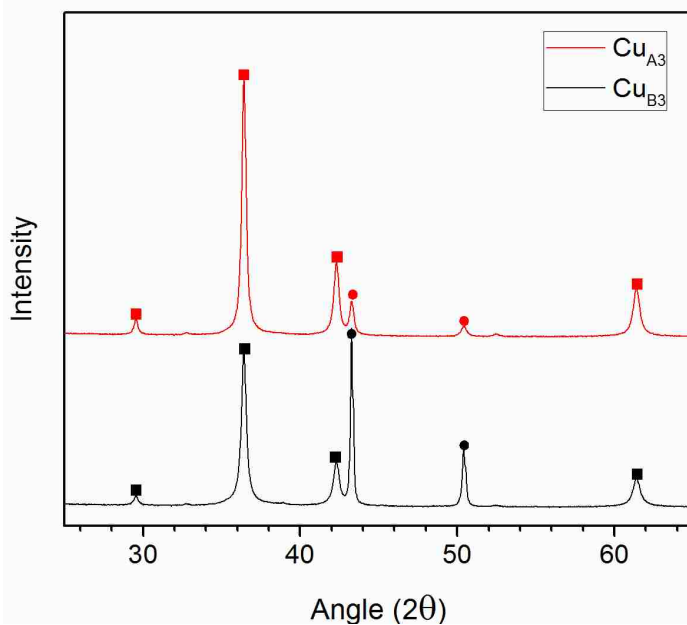


**Figure 23.** XRD patterns of catalysts prepared from 20wt% Cu precursors in 7% ( $\text{Cu}_{\text{A}3}$ , red) and 100%  $\text{H}_2$  ( $\text{Cu}_{\text{B}3}$ , black) atmospheres.  $\text{Cu}_2\text{O}$  (squares):  $29.6^\circ$  - (110),  $36.4^\circ$  - (111),  $42.3^\circ$  - (200),  $61.4^\circ$  - (220). Cu (circles):  $43.2^\circ$  - (111),  $50.4^\circ$  - (200). CuO is a minor phase included in refinements for the particles reduced in 100%  $\text{H}_2$ , at 12.1 mol%.

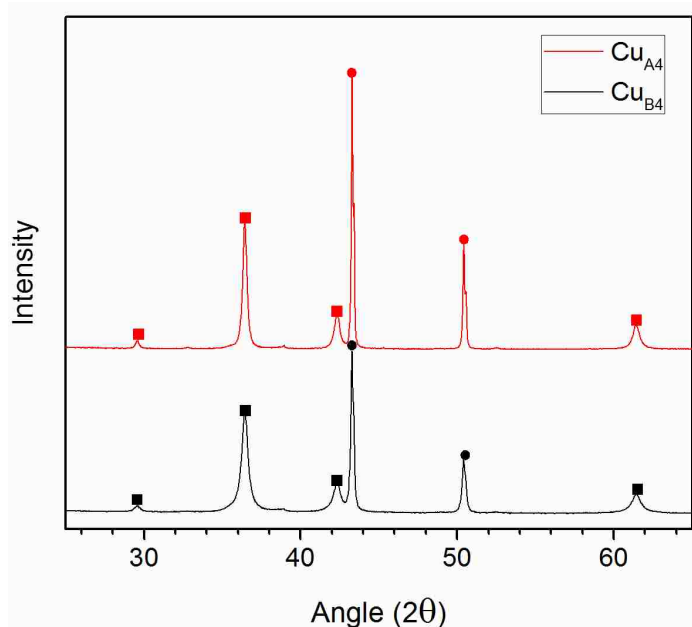


**Figure 24.** XRD patterns of catalysts prepared from 30wt% Cu precursors in 7% ( $\text{Cu}_{\text{A}4}$ , red) and 100%  $\text{H}_2$  ( $\text{Cu}_{\text{B}4}$ , black) atmospheres.  $\text{Cu}_2\text{O}$  (squares):  $29.6^\circ$  - (110),  $36.4^\circ$  - (111),  $42.3^\circ$  - (200),  $61.4^\circ$  - (220). Cu (circles):  $43.2^\circ$  - (111),  $50.4^\circ$  - (200). CuO was not detected as a minor phase.



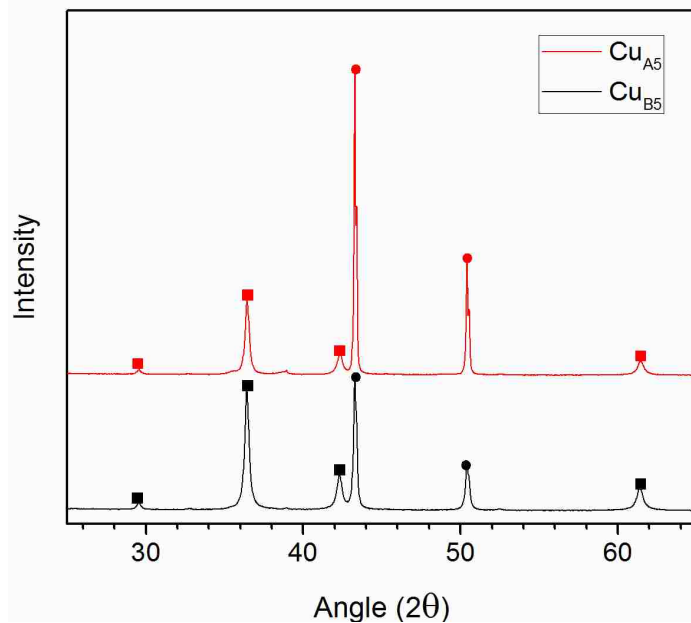


**Figure 25.** XRD patterns of catalysts prepared from 40wt% Cu precursors in 7% ( $\text{Cu}_{A5}$ , red) and 100%  $\text{H}_2$  ( $\text{Cu}_{B5}$ , black) atmospheres.  $\text{Cu}_2\text{O}$  (squares):  $29.6^\circ$  - (110),  $36.4^\circ$  - (111),  $42.3^\circ$  - (200),  $61.4^\circ$  - (220). Cu (circles):  $43.2^\circ$  - (111),  $50.4^\circ$  - (200). CuO is a minor phase included in refinements for the particles reduced in 7%  $\text{H}_2$ , at 4.61 mol%.

**Appendix 3.** Confirmation of CO<sub>2</sub> electroreduction on Cu nanoparticles with cyclic voltammetry at 20 mV s<sup>-1</sup> in N<sub>2</sub> and CO<sub>2</sub> saturated 0.1M KHCO<sub>3</sub> solutions.

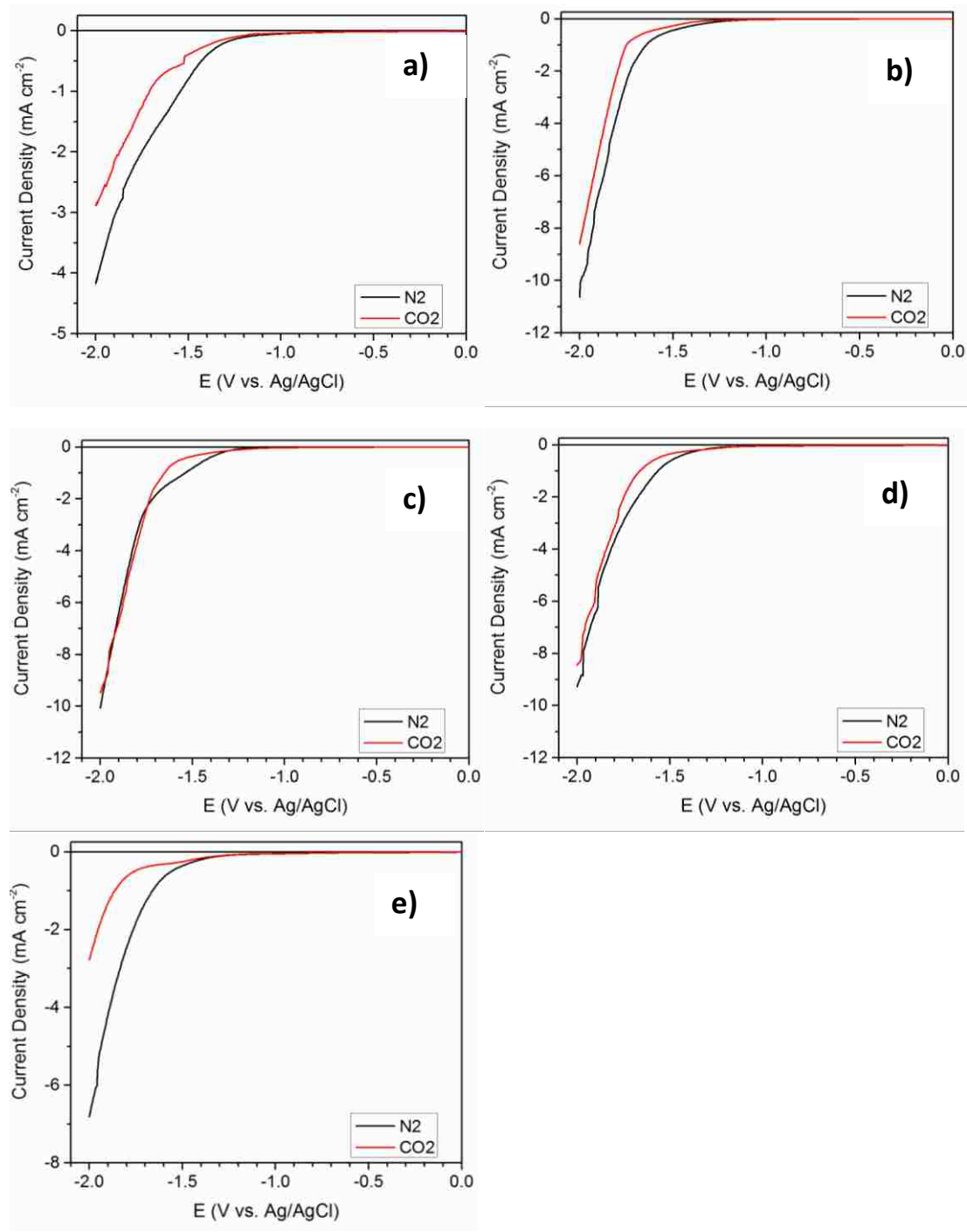


**Figure 26.** Confirmation of CER activity by comparison of cathodic voltammograms of Cu nanoparticles reduced at 350 °C in 7% H<sub>2</sub>. Conditions: N<sub>2</sub> or CO<sub>2</sub> saturated 0.1M KHCO<sub>3</sub>, 1600 RPM, 25°C. Particles are as follows: a) Cu<sub>A1</sub>, b) Cu<sub>A2</sub>, c) Cu<sub>A3</sub>, d) 3 Cu<sub>A4</sub>, and e) Cu<sub>A5</sub>.

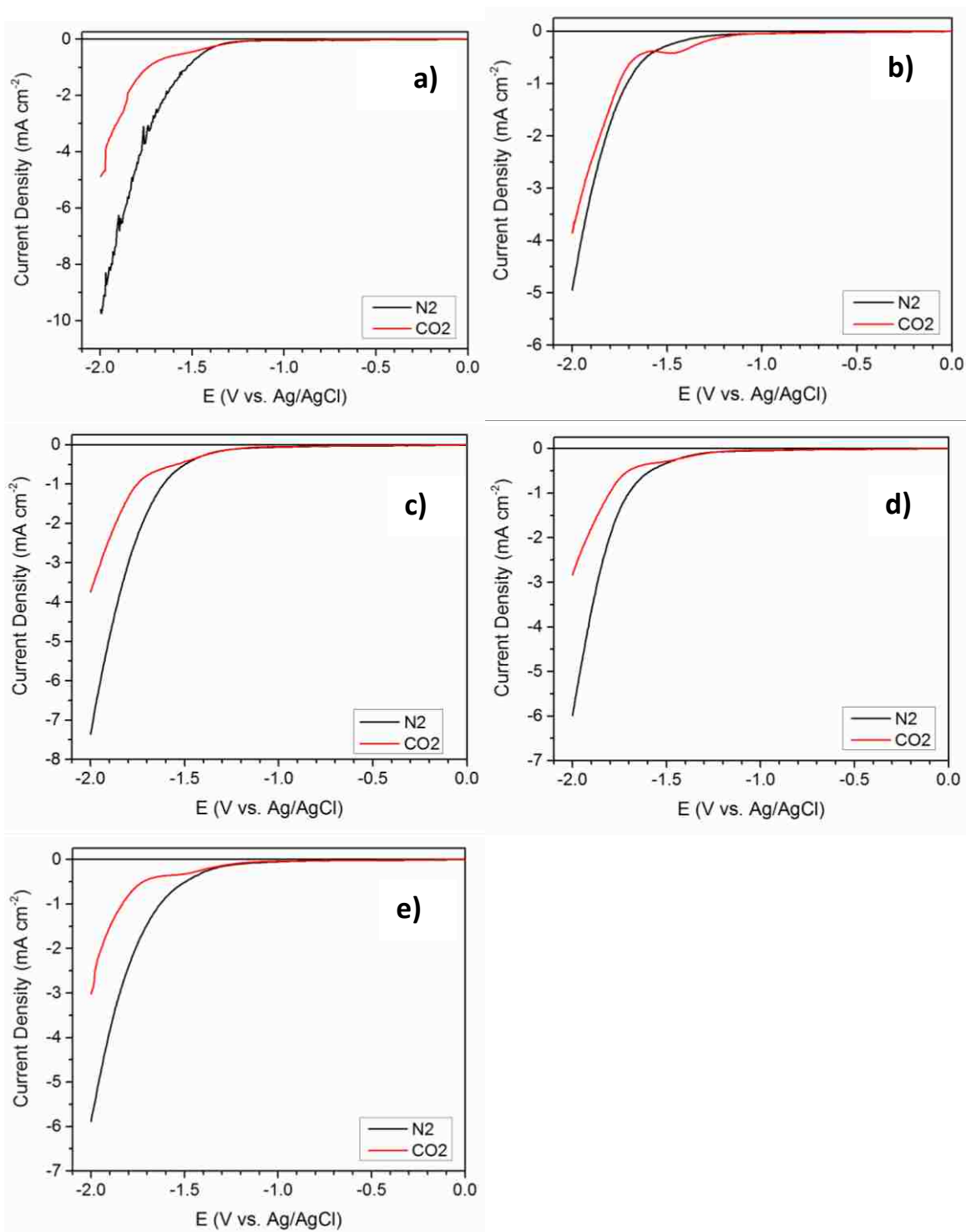


**Figure 27.** Confirmation of CER activity by comparison of cathodic voltammograms of Cu nanoparticles reduced at 250°C in 100% H<sub>2</sub>. Conditions: N<sub>2</sub> or CO<sub>2</sub> saturated 0.1M KHCO<sub>3</sub>, 1600 RPM, 25°C. Particles are as follows: a) Cu<sub>B1</sub>, b) Cu<sub>B2</sub>, c) Cu<sub>B3</sub>, d) 3 Cu<sub>B4</sub>, and e) Cu<sub>B5</sub>.

**Appendix 4.** Bulk electrolysis for carbon dioxide electroreduction of Cu nanoparticles held for one hour at -1.6 and -2.2 V vs. Ag/AgCl in 0.1M KHCO<sub>3</sub>, without rotation.

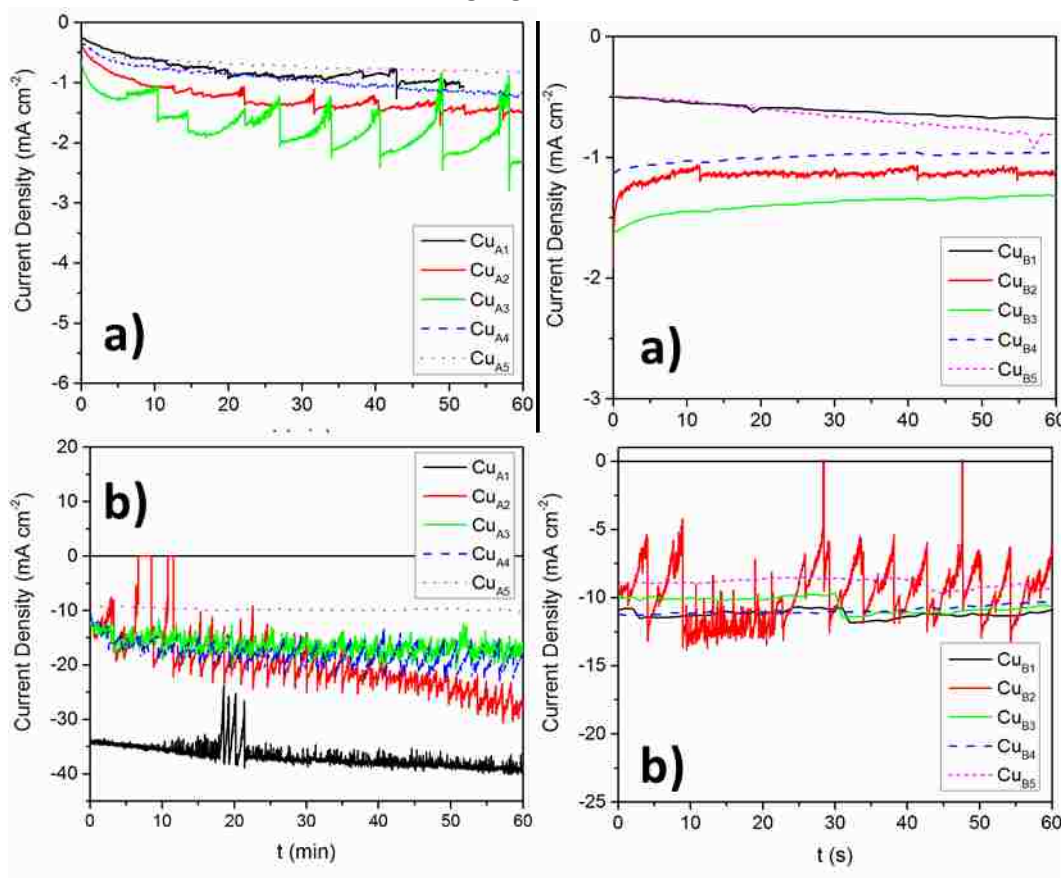


**Figure 28.** Bulk electrolysis of Cu<sub>A<sub>X</sub></sub> (X=1-5) particles reduced at 350°C in a 7% H<sub>2</sub> atmosphere at a) -1.6 and at b) -2.2 V vs. Ag/AgCl. Conditions: 0.1 M KHCO<sub>3</sub>, 1600 RPM, 25°C. Large spikes in current densities are caused by coverage of the working electrode surface by gas.

**Figure 29.** Bulk electrolysis of Cu<sub>B<sub>X</sub></sub> (X=1-5) particles reduced at 250°C in a 100% H<sub>2</sub> atmosphere at a) -1.6 and at b) -2.2 V vs. Ag/AgCl. Conditions: 0.1 M KHCO<sub>3</sub>, 1600 RPM, 25°C. Large spikes in current densities are caused by coverage of the working electrode surface by gas.

## References

1. United States Information Administration, *Monthly Energy Review January 2015*, (2015). <http://www.eai.gov/totalenergy> (accessed on January 10, 2015).
2. Ewald, J., *Carbon dioxide at NOAA's Mauna Loa Observatory Reaches New Milestone: Tops 400 ppm*. National Oceanic and Atmospheric Administration, 2013.
3. Lackner, K.S., *Carbonate Chemistry for Sequestering Fossil Carbon*. *Annu. Rev. Energy Environ.*, 27 (2002), 193-232.
4. Cramer, W.; Yohe, W.; Auffhammer, M.; Huggel, C.; Molau, U.; Silva Dias, M. A. F.; Solow, A.; Stone, D. A.; Tibig, L., *2014: Detection and attribution of observed impacts*. In *Climate Change 2014: Impacts, Adaptation, and Vulnerability. Part A: Global and Sectoral Aspects*. Contributions of Working Group II to the Fifth Assessment Report of the Intergovernmental Panel on Climate Change [Field, C. B.; Barros, V. R.; Dokken, D. J.; Mach, K. J., Mastrandrea, M. D.; Bilir, T. E.; Chatterjee, M.; Ebi, K. L.; Estrada, Y. O.; Genova, R. C.; Girma, B.; Kissel, E.S.; Levy, A. N.; MacCracken, S.; Mastrandrea, P. R.; White, L. L. (eds.)]. Cambridge University Press, Cambridge, United Kingdom and New York, N.Y., U.S.A., 979-1037.
5. Hoerling, M. P.; Eicheid, J.; Quan, X.; Diaz, H.; Webb, R.; Dole, R.; Easterling, D., *Is a Transition to Semipermanent Drought Conditions Imminent in the U.S. Great Plains?* *J. Climate*, 25 (2012), 8380-8386.
6. UNEP 2013, *The Emission Gap Report 2013*. United Nations Environmental Programme (UNEP), Nairobi.
7. Chakravarty, S.; Chikkatur, A.; Coninck, H.; Pacala, S.; Socolow, R.; Tavoni, M. *Sharing global CO<sub>2</sub> emissions reductions among one billion high emitters*. *Proc. Natl. Acad. Sci. U. S.A.*, 106 (2009), 11884-11888.
8. Sanchez-Sanchez, C. M.; Montiel, V.; Tryk, D.A.; Aldaz, A.; and Fujishima, A., *Electrochemical approaches to alleviation of the problem of carbon dioxide accumulation*. *Pure Appl. Chem.*, 73 (2001), 1917-1927.
9. Lim, R. J.; Zie, M.; Sk, M. A.; Lee, J. -M.; Fisher, A.; Wang, X.; and Lim, K. H., *A review on the electrochemical reduction of CO<sub>2</sub> in fuel cells, metal electrodes and molecular catalyt*. *Catal. Today*, 233 (2014), 169-180.
10. Lowry, D.; Jitaru, M., *Electroreduction of Carbon Dioxide in Electrochemically Enabled Sustainability: devices, materials, and mechanisms for energy conversion*; Chan K. -Y.; Li, C.-Y. V. Eds. Taylor & Francis Group, LLC, 2014, 1-54.
11. Delacourt, C.; and Newman, J., *Mathematical modeling of CO<sub>2</sub> reduction to CO in aqueous electrolytes II. Study of an electrolysis cell making syngas (CO+H<sub>2</sub>) from CO<sub>2</sub> and H<sub>2</sub>O at room temperature*. *J. Electrochem. Soc.*, 157 (2010), B1911-B1926.

12. Delacourt, C.; Ridgway, P.L.; Kerr, J.B.; and Newman J., *Design of an Electrochemical Cell Making Syngas (CO + H<sub>2</sub>) from CO<sub>2</sub> and H<sub>2</sub>O Reduction at Room Temperature*. J. Electrochem. Soc., 155 (2008), B42-B49.
13. Dufek, E. J.; Lister, T.E.; and McIlwain, M. E., *Bench-scale electrochemical system for generation of CO and syn-gas*. J. Appl. Electrochem., 41 (2011), 623-631.
14. Azuma, M.; Hashimoto, K.; and Hiramoto, M., *Electrochemical reduction of carbon dioxide on various metal electrodes in low-temperature aqueous KHCO<sub>3</sub> media*. J. Electrochem. Soc., 137 (1990), 1772-1778.
15. Azuma, M.; Hashimoto, K.; Hiramoto, M.; Watanabe, M.; Sakata, T., *Carbon dioxide reduction at low temperature on various metal electrodes*. J. Electroanal. Chem., 260 (1989), 441-445.
16. Bandi, A. and Kuhne, H. -M., *Electrochemical Reduction of Carbon Dioxide in Water: Analysis of the Reaction Mechanism on Ruthenium-Titanium-Oxide*. J. Electrochem. Soc., 139 (1992), 1605-1610.
17. Benson, E. E.; Kubiak, C. P.; Sathrum, A.J.; and Smieja, J. M., *Electrocatalytic and homogeneous approaches to conversion of CO<sub>2</sub> to liquid fuels*. Chem. Soc. Rev., 28 (2009), 89-99.
18. Chen, Y.; and Kanan, M.W., *Tin oxide dependence of the CO<sub>2</sub> reduction efficiency on tin electrode and enhanced activity for tin/tin oxide thin-film catalysts*. J. Am. Chem. Soc., 134 (2012), 1986-1989.
19. Chen, Y.; Li, C. W.; Kanan, M. W., *Aqueous CO<sub>2</sub> Reduction at Very Low Overpotential on Oxide-derived Au Nanoparticles*. J. Am. Chem. Soc., 134 (2012), 19969-19972.
20. Hori, Y.; Kikuchi, K.; Suzuki, S., *Production of CO and CH<sub>4</sub> in aqueous hydrogencarbonate solution*. Chem. Lett., 1985, 1695-1698.
21. Hori, Y.; Kikuchi, K.; Murata, A.; Suzuki, S., *Production of Methane and Ethylene in Electrochemical Reduction of Carbon Dioxide at Copper Electrode in Aqueous Hydrogencarbonate Solution*. Chem. Lett., 1986, 897-898.
22. Hori, Y.; Murata, A.; Takahashi, R., *Formation of Hydrocarbons in the Electrochemical Reduction of Carbon Dioxide at a Copper Electrode in Aqueous Solutions*. J. Chem. Soc. Faraday Trans. 1, 85 (1989), 2309-2326.
23. Hori, Y.; Wakebe, H.; Tsukamoto, T.; Koga, O., *Electrocatalytic process of CO selectivity in electrochemical reduction of CO<sub>2</sub> at metal electrodes in aqueous media*. Electrochim. Acta, 39 (1994), 1833-1839.
24. Hori, Y. in *Modern Aspects of Electrochemistry*; Vayenas, C. G., White, R.E., Gamboa-Aldeco, M.E., Eds; Springer: New York, NY, 2008; Vol. 42.

25. Januszewska, A.; Jurczakowski, R.; and Kulesza, P. J., *CO<sub>2</sub> electroreduction at bare and Cu-decorated Pd pseudomorphic layers: Catalyst tuning by controlled and indirect supporting on Au (111)*. *Langmuir*, 30 (2014), 14314-14321.
26. Jitaru, M.; Lowy, D. A.; Toma, M.; Toma, B. C.; Oniciu, L., *Electrochemical reduction of carbon dioxide on flat metallic cathodes*. *J. Appl. Electrochem.*, 27 (1997), 875-889.
27. Kudo, A.; Nakagawa, S.; Tsuneto, A.; Sakata, T., *Electrochemical Reduction of High Pressure CO<sub>2</sub> on Ni Electrodes*. *J. Electrochem. Soc.* 140 (1993), 1541-1545.
28. Tomita, Y.; Teruya, S.; Koga, O.; Hori, Y., *Electrochemical Reduction of Carbon Dioxide at a Platinum Electrode in Acetonitrile-water Mixtures*. *J. Electrochem. Soc.* 147 (2000), 4164-4167.
29. Huang, T.-J.; Chou, C.-L., *Electrochemical CO<sub>2</sub> reduction with power generation in SOFCs with Cu-added LSCF-GDC cathode*. *Electrochemistry Communication*, 11 (2009), 1464-1467.
30. Zhan, Z.; Zhao, L., *Electrochemical reduction of CO<sub>2</sub> in solid oxide electrolysis cells*. *J. Power Sources*, 195 (2010), 7250-7254.
31. Whippel, D. *Microfluidic platform for studying the electrochemical reduction of carbon dioxide*. (Unpublished doctoral thesis), University of Illinois: Urbana-Champaign, Illinois, 2011.
32. Whippel, D. T.; and Kenis, P. J., *Prospects of CO<sub>2</sub> Utilization via Direct Heterogeneous Electrochemical Reduction*. *J. Phys. Chem. Lett.*, 1 (2010), 3451-3458.
33. Jhong, H. -R.; Ma, S.; and Kenis, P. J., *Electrochemical conversion of CO<sub>2</sub> to useful chemicals: current status, remaining challenges, and future opportunities*. *Current Opinion in Chemical Engineering*, Yang, H. and Zeng, H.C. Ed., 2 (2013), 191-199.
34. Hori, Y.; Takagashi, I.; Koga, O.; and Hoshi, N., *Selective Formation of C<sub>2</sub> Compounds from Electrochemical Reduction of CO<sub>2</sub> at a series of Copper Single Crystal Electrodes*. *J. Phys. Chem. B.*, 106 (2002), 15-17.
35. Hori, Y.; Takagashi, I.; Koga, O.; and Hoshi, N., *Electrochemical reduction of carbon dioxide at various series of copper single crystal electrodes*. *J. Mol. Catal. A*, 199 (2003), 39-47.
36. Innocent, B.; Pasquier, D.; Ropital, F.; Hahn, F.; Leger, J.-M.; and Kokoh, K. B., *FTIR spectroscopy study of the reduction of carbon dioxide on lead electrode in aqueous medium*. *Appl. Catal. B-Environ.*, 94 (2010), 219-224.
37. Kuhl, K. P.; Cave, E. R.; Abram, D. N.; and Jaramillo, T. F., *New insights into the electrochemical reduction of carbon dioxide on metallic copper surfaces*. *Energy Environ. Sci.*, 5 (2012), 7050-7059.
38. Peterson, A. A.; and Norskov, J. K., *Activity Descriptors for CO<sub>2</sub> Electroreduction to Methane on Transition metal catalysts*. *J. Phys. Chem. Lett.*, 3 (2012), 251-258.

39. Peterson, A. A.; Abild-Pedersen, F.; Studt, F.; Rossmeisl, J.; and Norskov, J. K., *How copper catalyzes the electroreduction of carbon dioxide into hydrocarbon fuels*. Energy Environ. Sci., 3 (2010), 1311-1315.
40. Reske, R.; Mistry, H.; Behafarid, F.; Cuenya, B. R.; and Strasser, P., *Particle size effects in the catalyst electroreduction of CO<sub>2</sub> on Cu nanoparticles*. J. Am. Chem. Soc. 136 (2014), 6978-6986.
41. Andersen, N.; Serov, A.; and Atanassov, P., *Metal oxides/CNT nano-composite catalyst for oxygen reduction/oxygen evolution in alkaline media*. Appl. Catal. B-Environ., 163 (2015), 632-627.
42. Baturina, O.; Lu, Q.; Padilla, M.; Le, X.; Li, W.; Serov, A.; Artyushkova, K.; Atanassov, P.; Xu, F.; Epshteyn, A.; Brintlinger, T.; Schuette, M.; and Collins, G., *CO<sub>2</sub> Electroreduction to Hydrocarbons on Carbon-Supported Cu Nanoparticles*. ACS Catal., 4 (2014), 3682-3695.
43. Gupta, N.; Gattrell, M.; and MacDougall, B., *Calculations for the cathode surface concentrations in the electrochemical reduction of CO<sub>2</sub> in KHCO<sub>3</sub> solutions*. J. Appl. Electrochem., 36 (2006), 161-172.
44. Hara, K.; Tsuneto, A.; Kudo, A.; Sakata, T., *Electrochemical Reduction of CO<sub>2</sub> on a Cu Electrode under High Pressure*. J. Electrochem. Soc., 141 (1994), 2097-2103.
45. Hara, K.; Kudo, A.; Sakata, T., *Electrochemical reduction of carbon dioxide under high pressure on various electrodes in an aqueous electrolyte*. J. Electroanal. Chem., 391 (1995), 141-147.
46. Wu, H.; Zhang, N.; Wang, H.; Hong, S., *Adsorption of CO<sub>2</sub> on Cu<sub>2</sub>O (111) oxygen-vacancy surface: First-principles study*. Chem. Phys. Lett. 568-569 (2013), 84-89.
47. Kas, R.; Kortlever, R.; Millbrat, A.; Koper, M.T.; Mul, G.; and Baltrusaitis, J., *Electrochemical CO<sub>2</sub> reduction on Cu<sub>2</sub>O derived copper nanoparticles- controlling the catalytic selectivity of hydrocarbons*. Phys. Chem. Chem. Phys., 16 (2014), 12194-12201.
48. Sen, S.; Lui, D.; and Palmore, G. T. R., *Electrochemical reduction of CO<sub>2</sub> at copper nanofoams*. ACS Catal., 4 (2014), 3091-3095.
49. Bard, A. and Faulkner, L., *Electrochemical Methods: Fundamentals and Applications*. 2nd Ed., 2001, John Wiley & Sons, U.S.A.
50. Li, C. W.; Kanan, M. W., *CO<sub>2</sub> Reduction at Low Overpotential on Cu Electrodes Resulting from the Reduction of Thick Cu<sub>2</sub>O Films*. J. Am. Chem. Soc., 134 (2012), 7231-7234.
51. Li, C. W.; Ciston, J.; Kanan, M. W., *Electroreduction of carbon monoxide to liquid fuel on oxide-derived nanocrystalline copper*. Nature, 507 (2014), 504-507.
52. Jordan, J.; Smith, P. T., *Free-Radical Intermediate in the Electroreduction of Carbon Dioxide*. Proc. Chem. Soc., 44 (1960), 246-247.



53. Gennaro, A.; Isse, A. A.; Vianello, E. *Solubility of electrochemical determination of CO<sub>2</sub> in some dipolar aprotic solvents*. J. Electroanal. Chem., 289 (199), 203-215.
54. Tang, W.; Peterson, A. A.; Varela, A. S.; Jovanov, Z. P.; Bech, L.; Durand, W.J.; Dahl, S.; Norskov, J. K.; and Chorkendorff, I., *The importance of surface morphology in controlling the selectivity of polycrystalline copper for CO<sub>2</sub> electroreduction*. Phys. Chem. Chem. Phys., 14 (2012), 76-81.
55. Wanatabe, M.; Shibata, M.; Kato, A.; Azuma, M.; and Sakata, T., *Design of Alloy electrocatalyst for CO<sub>2</sub> reduction III. The selective and reversible reduction of Cu alloy electrodes*. J. Electrochem. Soc., 138 (1991), 3382-3389.
56. Kim, D.; Resasco, J.; Yu, Y.; Asiri, A. M.; and Yang, P., *Synergistic geometric and electronic effects for electrochemical reduction of carbon dioxide using gold-copper bimetallic nanoparticles*. Nat. Commun., 5 (2014), doi:10.1038/ncomms5948.
57. Hossain, S. S.; Rahman, S. U.; Ahmed, S., *Electrochemical Reduction of Carbon Dioxide over CNT-Supported Nanoscale Copper Electrocatalysts*. Journal of Nanomaterials, 2014, 2014, 10 pages, doi:10.1155/2014/374318.
58. Keil, P.; Lutzenkirchen-Hecht, D.; Frahm, R. *Investigation of room temperature oxidation of Cu in air by Yoneda-XAFS*. AIP Conf. Proc. 882 (2007), <http://dx.doi.org/10.1063/1.2644569>
59. Ishizaki, T.; Watanabe, R. *A new one-pot method for the synthesis of Cu nanoparticles for low temperature bonding*. J. Mater. Chem., 22 (2012), 25198-25206.
60. Park, B. K.; Jeong, S.; Kim, D., Moon, J., Lim, S., Kim, J. S. *Synthesis and size control of monodisperse copper nanoparticles by polyol method*. Journal of Colloid and Interface Science, 311 (2007), 417-424.
61. Stern, K. *High Temperature Properties and Decomposition of Inorganic Salts Part 3. Nitrates and Nitrites*. J. Phys. Chem. Ref. Data, 1 (1972), 747-772.
62. L'vov, B. V.; Novichikhin, A. V. *Mechanism of thermal decomposition of hydrated copper nitrate in vacuo*. Spectrochim. Acta B, 50 (1995), 1459-1468.
63. L'vov, B. V.; Novichikhin, A.V. *Mechanism of thermal decomposition of anhydrous metal nitrates*. Spectrochim. Acta B, 50 (1995), 1427-1448.
64. Ryu, S. K.; Lee, W. K.; and Park, S. J., *Thermal Decomposition of Hydrated Copper Nitrate [Cu(NO<sub>3</sub>)<sub>2</sub> • 3H<sub>2</sub>O] on Activated Carbon Fibers*. Carbon Science, 5 (2004), 180-185.
65. Hori, Y.; Konishi, H.; Futamura, T.; Murata, A.; Koga, O.; Sakurai, H.; Oguma, K., *"Deactivation of copper electrode" in electrochemical reduction of CO<sub>2</sub>*. Electrochim. Acta, 50 (2005), 5354-5369.
66. *Potassium biocarbonate ACS reagent grade*; MSDS No. 237205 [online]; Sigma-Aldrich, St. Louis, MO; 11/2010.

[http://www.sigmaaldrich.com/Graphics/CO2Info/SigmaSAPQM/SPEC/23/237205/237205-BULK\\_\\_\\_\\_\\_SIAL\\_\\_\\_\\_\\_.pdf](http://www.sigmaaldrich.com/Graphics/CO2Info/SigmaSAPQM/SPEC/23/237205/237205-BULK_____SIAL_____.pdf) (accessed February 28, 2015).

66. Hara, K.; Kudo, A.; Sakata, T., *Electrochemical CO<sub>2</sub> reduction on a glassy carbon electrode under high pressure*. J. Electroanal. Chem., 42 (1997), 1-4.
67. Kyriacou, G. Z.; and Anagnostopoulous, A. K., *Influence of CO<sub>2</sub> partial pressure and the supporting electrolyte cation on the product distribution of CO<sub>2</sub> electroreduction*. J. Appl. Electrochem., 23 (1993) 483-486.
68. Nakagawa, S.; Kudo, A.; Azuma, M.; Sakata, T., *Effect of pressure on the electrochemical reduction of CO<sub>2</sub> on Group VIII metal electrodes*. J. Electroanal. Interfacial Electrochem. 308 (1991), 339-343.
69. Todoroki, M.; Hara, K.; Kudo, A.; Sakata, T., *Electrochemical reduction of high pressure CO<sub>2</sub> at Pb, Hg, and In electrodes in aqueous KHCO<sub>3</sub> solution*. J. Electroanal. Chem., 394 (1995), 199-203.
70. Smith, F.; Harvey, A. H., *Avoid Common Pitfalls When Using Henry's Law*. Chem. Eng. Proc., (2007), 33-39.
71. Beverskog, B.; Puigdomenech, I., *Revised Pourbaix Diagrams for Copper at 5-150 °C*. 1995, Site-94. Nykoping Sweden.
72. Wanatabe, M.; Shibata, M.; Kato, A.; Azuma, M.; and Sakata, T., *Design of Alloy electrocatalyst for CO<sub>2</sub> reduction III. The selective and reversible reduction of Cu alloy electrodes*. J. Electrochem. Soc., 138 (1991), 3382-3389.
73. Serov, A.; Martinez, U.; Falase, A.; Atanassov, P., *Highly Active PdCu catalysts for electrooxidation of 2-propanol*. Electrochem. Comm., 22 (2012), 193-196.
74. Falase, A.; Main, M.; Garcia, K.; Serov, A.; Lau, C.; Atanassov, P., *Electrooxidation of ethylene glycol and glycerol by platinum-based binary and ternary nano-structured catalysts*. Electrochim. Acta 66 (2012) 295-301.
75. Pylypenko, S.; Mukherjee, S.; Olson, T. S.; Atanassov, P. *Non-platinum oxygen reduction electrocatalysts based on pyrolyzed transition metal macrocycles*. Electrochim. Acta 53 (2008), 7875-7883.
76. Robson, M. H.; Serov, A.; Artyushkova, K.; Atanassov P. *A mechanistic study of 4-aminoantipyrine and iron derived non-platinum group metal catalyst on the oxygen reduction reaction*. Electrochim. Acta, 90 (2013), 656-665.
77. Brocato, S.; Serov, A.; Atanassov P. *pH dependence of catalytic activity for ORR of the non-PGM catalyst derived from heat-treated Fe-phenanthroline*. Electrochim. Acta, 87 (2013), 361-365.
78. Serov, A.; Robson, M. H.; Artyushkova, K.; Atanassov, P. *Templated non-PGM cathode catalysts derived from iron and poly(ethyleneimine) precursors*. Appl. Catal. B, 127 (2012), 300-306.

79. Serov, A.; Robson, M. H.; Smolnik, M.; Atanassov P., *Templated bi-metallic non-PGM catalysts for oxygen reduction*. *Electrochim. Acta*, 80 (2012), 213-218.
80. Serov, A.; Robson, M. H., Halevi, B.; Artyushkova, K.; Atanassov, P., *Highly active and durable template non-PGM cathode catalysts derived from iron and aminoantipyrine*. *Electrochem. Comm.*, 22 (2012), 53-56.
81. Serov, A.; Martinez, U.; Atanassov, P., *Novel Pd-In catalysts for alcohols electrooxidation in alkaline media*. *Electrochem. Comm.*, 34 (2013), 185-188.
82. Serov, A.; Robson, M. H.; Smolnik, M.; Atanassov, P., *Tri-metallic transition metal-nitrogen-carbon catalysts derived by sacrificial support method synthesis*. *Electrochim. Acta*, 109 (2013), 433-439.